CHEMPHYSCHEM

Femtochemistry of Norrish Type-I Reactions: II. The Anomalous Predissociation Dynamics of Cyclobutanone on the S_1 Surface

Eric W.-G. Diau, Carsten Kötting, and Ahmed H. Zewail*[a]

The anomalous nonradiative dynamics for three cyclobutanone isotopomers ([D_0]-, 3,3-[D_2]-, and 2,2,4,4-[D_4]cyclobutanone) have been investigated using femtosecond (fs) time-resolved mass spectrometry. We have found that the internal motions of the molecules in the S_1 state above the dissociation threshold involve two time scales. The fast motion has a time constant of < 50 fs, while the slow motion has a time constant of 5.0 ± 1.0, 9.0 ± 1.5, and 6.8 ± 1.0 ps for the [D_0], [D_2], and [D_4] species, respectively. Density functional theory and ab initio calculations have been performed to characterize the potential energy surfaces for the S_0, $S_1(n,\pi^*)$, and $T_1(n,\pi^*)$ states. The dynamic picture for bond breakage is the following: The fast motion represents the rapid dephasing of the initial wave packet out of the Franck–Condon region, whereas the slow motion reflects the α-cleavage dynamics of the Norrish type-I reaction. The redistribution of the internal energy from the initially activated out-of-plane bending modes into the in-plane ring-opening reaction coordinate defines the time scale for intramolecular vibrational energy redistribution (IVR), and the observed picosecond-scale (ps) decay gives the rate of IVR/bond cleavage across the barrier. The observed prominent isotope effect for both [D_2] and [D_4] isotopomers imply the significance of the ring-puckering and the CO out-of-plane wagging motions to the S_1 α-cleavage dynamics. The ethylene and ketene (C_2 products)—as well as CO and cyclopropane (C_3 products)—product ratios can be understood by the involvement of an S_0/S_1 conical intersection revealed in our calculations. This proposed dynamic picture for the photochemistry of cyclobutanone on the S_1 surface can account not only for the abnormally sharp decrease in fluorescence quantum yield and lifetime but also for the dramatic change in the C_3:C_2 product ratio as a function of increasing excitation energy, as reported by Lee and co-workers (J. C. Hemminger, E. K. C. Lee, J. Chem. Phys. ***1972***, 56, *5284–5295; K. Y. Tang, E. K. C. Lee,* J. Phys. Chem. ***1976***, 80, *1833–1836).*

KEYWORDS:

conical intersections · cyclobutanone · femtochemistry · mass spectrometry · Norrish reactions

1. Introduction

The Norrish type-I reaction is an important and common photochemical process in which the excitation of ketones leads to the CC σ-bond cleavage at the α position of the excited carbonyl group (α-cleavage).[1–3] This process produces a radical pair from a noncyclic ketone but a diradical intermediate from a cyclic ketone, and the overall reaction involves multiple chemical bond breaking and formation events. The mechanistic and dynamic features of this prototype reaction have been a fundamental subject of many detailed investigations, both experimentally and theoretically, over many decades.[1, 4–8]

Among all the aliphatic ketones previously studied, cyclobutanone (CB) is strikingly a special case because its photochemical behavior differs significantly from that of noncyclic and other cyclic ketones of larger ring sizes.[9, 10] In CB, the release of the ring-strain energy during α-cleavage in the S_1 excited state increases the exothermicity between the excited state and the acyl diradical intermediate. Thus, CB is expected to have a lower activation energy in the excited state than the other large-ring cyclic ketones according to the Hammond postulate.[11] The unusual photochemical behavior due to the "ring-strain effect" of the four-membered ring molecule was also demonstrated using a simple qualitative state-correlation diagram initially introduced by Salem.[12, 13] As a result, many important features for the photophysical and photochemical behavior of CB have been reported including work on photochemistry studies in solution,[4, 9] conventional product and lifetime measurements,[14] jet-cooled spectroscopy studies,[15, 16] and the product state-distribution investigation.[17]

The first singlet electronic transition of CB is characterized by a weak and broad absorption band from 330 to 240 nm with its maximum around 280 nm.[18, 19] This weak $S_0 \rightarrow S_1$ absorption feature, arising from a symmetry-forbidden $n \rightarrow \pi^*$ transition ($\tilde{A}^1A_2 \leftarrow \tilde{X}^1A_1$), is common to the entire class of carbonyl compounds.[4] The initial photophysical transformation of CB near the onset of the $S_0 \rightarrow S_1$ excitation ($\lambda_{ex} \sim 330$ nm) has been proposed to result in the $S_1 \rightarrow S_0$ fluorescence, undergo intersystem crossing (ISC) to the lowest triplet state (T_1), and

[a] *Prof. A. H. Zewail, Dr. E. W.-G. Diau, Dr. C. Kötting*
Arthur Amos Noyes Laboratory of Chemical Physics
California Institute of Technology
Pasadena, CA 91125 (USA)
Fax: (+1)626-792-8456
E-mail: zewail@caltech.edu

internally convert to the hot ground state (S_0^*).[10] Since the fluorescence quantum yield (Φ_F) is only $\sim$0.002 at excitation wavelengths above 320 nm,[14e] the primary S_1 relaxation at longer wavelengths is dominated by nonradiative processes, especially due to the efficient $S_1 \rightarrow T_1$ intersystem crossing as in the case of acetone.[1, 20] Such nonradiative transition is predominant for the primary photoprocess of CB near the $S_0 \rightarrow S_1$ absorption threshold and governs the observed S_1 lifetime (τ_S) in this wavelength range. Interestingly, τ_S is almost constant for most aliphatic ketones at $\lambda_{ex} = 320 - 330$ nm and it is also insensitive to changes of solvent,[14c,d] which suggests that the rates of the nonradiative relaxation ($=\tau_S^{-1}$) are intrinsic and not affected by the media. For CB at $\lambda_{ex} > 320$ nm, τ_S is approximately 4.5 ns.[14e] However, both Φ_F and τ_S of CB decrease drastically at excitation wavelengths shorter than $\sim$320 nm, indicating the opening of a new, rapid, nonradiative channel corresponding to a molecular predissociation process for $\lambda_{ex} < 320$ nm.[14e] This photochemical behavior of CB contrasts with that of most other ketones studied before.[1]

Early studies have also demonstrated that there are two major reaction channels involved in the photodecomposition of cyclobutanone upon excitation to the $S_1(n,\pi^*)$ state, Equation (1).[14]

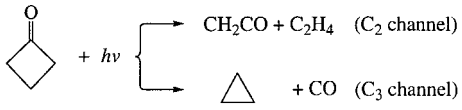

(1)

The C_2 channel produces two-carbon atom products ketene (CH_2CO) and ethylene (C_2H_4) whereas the C_3 channel produces vibrationally excited cyclopropane (*cyclo*-C_3H_6) and CO. The other minor C_3 channel product, propylene (C_3H_6), has been shown to be produced via secondary isomerization of the vibrationally hot *cyclo*-C_3H_6.[21] Therefore, the overall product yield of the C_3 channel is the sum of both *cyclo*-C_3H_6 and C_3H_6. An early benzene photosensitization study demonstrated that the T_1 state of CB generates almost exclusively cyclopropane and CO via the C_3 channel, whereas ketene and ethylene produced via the C_2 channel are from the S_1 state.[14a] Therefore, the C_3:C_2 product ratio is related to the decay rate of the S_1 state (due to internal conversion or predissociation process) over that of the T_1 state (due to intersystem crossing). The value of the C_3:C_2 ratio drops dramatically as the excitation shifts from longer wavelengths ($\sim$7:1 at $\lambda_{ex} \sim 340$ nm) to around the predissociation threshold region ($\sim$0.5:1 at $\lambda_{ex} \sim 315$ nm).[14f] Beyond this region for excitation wavelengths shorter than $\sim$315 nm, the C_3:C_2 ratio was observed to be relatively insensitive to the wavelength. The sharp variation of the C_3:C_2 ratio in the predissociation threshold region is consistent
with the change of the Φ_F and τ_S in the similar wavelength range. These branching-ratio results further confirm that the newly opened nonradiative channel is in nature an $S_1 \rightarrow S_0$ internal conversion process, which eventually leads to the C_2 products.

Detailed investigations[15, 16] of the jet-cooled fluorescence excitation spectra of CB in the wavelength region 305 – 335 nm have provided important information for understanding the structure and the dynamic behavior of CB in the $S_1(n,\pi^*)$ state. Based upon the observed spectral data, a two-dimensional potential energy function was proposed with two active vibrational modes corresponding to the CO out-of-plane wagging and the ring-puckering motions.[16a] The barrier to inversion of the CO wagging motion in CB was determined to be $\sim$6 kcal mol^{-1} with the equilibrium wagging angle of $\sim 40^\circ$. The appreciable increase of the inversion barrier in cyclobutanone ($\sim$6 kcal mol^{-1}, as compared to $\sim$2 kcal mol^{-1} in cyclopentanone)[15, 22] indicates that the strain of the four-membered ring again plays a role in the chemistry of the S_1 excited state. The ring-puckering mode was found to be essentially barrierless with respect to planarity; the equilibrium puckering angle is $\sim 12^\circ$. Furthermore, the ring-puckering frequency of the S_1 state is much larger than that of the ground state (106 versus 36 cm^{-1}),[16] suggesting that the increase of the frequency upon excitation is related to the increasing interaction between a β-H atom and the p_x orbital of the carbonyl carbon atom by promoting a nonbonding electron to the antibonding orbital. Its consequence in the dynamic behavior of CB will be discussed later.

In earlier, extensive studies on the photochemistry of cyclobutanone, the following points were established: a) The primary photoprocess is nonradiative; b) CB behaves like other ketones at excitation wavelengths above 320 nm, where the $S_1 \rightarrow T_1$ ISC leading to the C_3 products dominates; c) The abnormal photochemical behavior of CB occurs at the excitation wavelength below 320 nm, where an $S_1 \rightarrow S_0$ predissociation channel was proposed to account for the predominant C_2 products; d) The equilibrium structure of the S_1 state is bent and the active vibrational modes are characterized by the CO out-of-plane wagging and the ring-puckering motions.

Several pertinent questions, which have been of interest of almost 30 years,[14e] need to be addressed: a) How rapid are the nonradiative processes ($S_1 \rightarrow T_1$ and $S_1 \rightarrow S_0$) compared to the direct chemical decomposition from the S_1 manifold, that is, what is the time scale for the mysterious predissociation channel above its threshold? b) What are the promoting vibronic modes of these intramolecular processes and their effect on the observed dynamics? c) Can a dynamic model be deduced to explain the observed results?

In this work, we report real-time observation of the Norrish type-I reaction dynamics for the α-cleavage of cyclobutanone in the $S_1(n,\pi^*)$ excited state studied in a molecular beam. Using femtosecond-resolved mass spectrometry, we investigated the initial motion of the nuclear wave packet and the actual rate corresponding to the nonradiative S_1 bond-dissociation process for three cyclobutanone isotopomers—[D_0]CB, 3,3-[D_2]cyclobutanone ([D_2]CB), and 2,2,4,4-[D_4]cyclobutanone ([D_4]CB). Density functional theory (DFT) and complete active space (CAS) self-consistent field (SCF) approaches were employed to characterize the global ground-state potential energy surface (PES) and the α-cleavage excited-state (S_1 and T_1) PESs.

Experimental Section

The experimental setup has been described in detail elsewhere.[54, 55] Briefly, the laser system contains a colliding-pulse mode-locked (CPM) laser pumped by an Ar^+ laser and then amplified by a four-stage, Nd:YAG-pumped amplifier operating at 20 Hz. The output of the fs laser source has a pulse width of $\sim$80 fs with pulse energy of $\sim$150 μJ at 615 nm. The pulse was split to provide the pump and probe beams. For the pump, the 615 nm output was frequency doubled. The probe beam was passed to a computer-controlled translation stage for the time delay. The instrumental response function was determined by in situ measurements.[54–56] The two beams were spatially combined and were focussed onto the supersonic molecular beam inside the vacuum chamber containing the TOF mass spectrometer. By gating the signal due to a particular ion and varying the delay time between pump and probe beams, the transient of each species was measured.

Cyclobutanone (99%, Aldrich) was used without further purification. The cyclobutanone isotopomers, $[D_2]$CB[57] and $[D_4]$CB,[58] were synthesized and purified prior to use. The molecular beams were formed by expanding gaseous CB seeded in He. The total stagnation pressure was varied and found to have no effect to the shape of the transients in the pressure range of 35 – 140 kPa. The pulse nozzle was heated to $\sim$130 °C to prevent clustering of molecules during expansion.

2. Results

Figure 1 shows the femtosecond mass spectra for $[D_0]$-, $[D_2]$-, and $[D_4]$CB. The spectrum of $[D_0]$CB shows only two prominent peaks, the parent ion at 70 amu and a fragment ion at 42 amu. Both spectra of $[D_2]$CB and $[D_4]$CB involve more peaks. The intense peaks at 72 and 74 amu are due to the $[D_2]$CB and $[D_4]$CB parent ions, respectively. The peak at 73 amu in the spectrum of $[D_4]$CB is due to the parent signal of the 2,2,4-$[D_3]$cyclobutanone isotopic impurity. For $[D_2]$CB, the peaks at 44 and 42 amu correspond to the $C_3H_4D_2$ ion and the C_2H_2O ion, respectively. Similarly, the peaks at 46 and 44 amu in the $[D_4]$CB spectrum correspond to the $C_3D_4H_2$ ion and C_2D_2O ion, respectively.

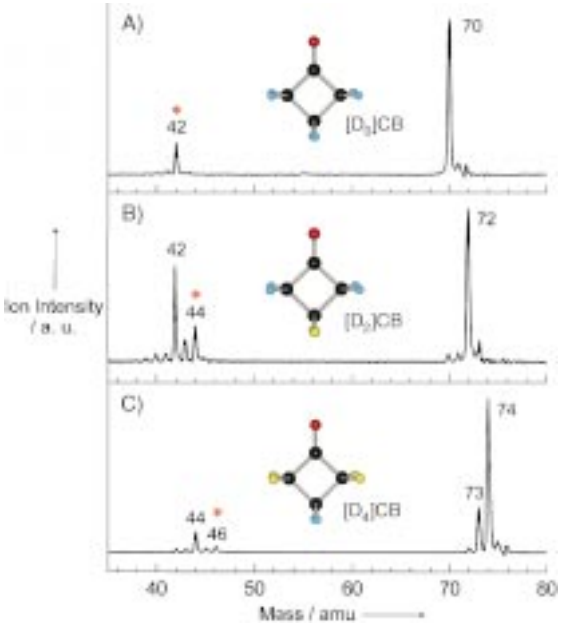

Figure 1. Femtosecond mass spectra of A) $[D_0]$cyclobutanone, B) 3,3-$[D_2]$cyclobutanone, and C) 2,2,4,4-$[D_4]$cyclobutanone. The spectra were obtained at a delay time of $\sim$50 fs between the pump and probe pulses. The stars (*) mark the masses used for obtaining the fragment transients.

Figures 2 A and 2 B display the fs transients and the corresponding pump-laser power dependence of the parent $[D_0]$CB ion signals (70 amu), respectively. In Figure 2 A, both transients were taken at the same pump intensity ($I_{pump} = 0.6$ μJ pulse^{-1}) but with different probe intensities (I_{probe}) fixed at the pulse energies of 2.3 μJ and 20 μJ as indicated. The transients were fitted by a single exponential decay function (time constant τ), convoluted with the instrumental response function (Gaussian, FWHM $\sim$170 fs), where $\tau = 80$ and 50 fs for I_{probe} at 2.3 and 20 μJ, respectively. Even though it is within the experimental uncertainties, there is also a small background offset component at the longer pump – probe delay time ($t \sim 1$ ps); for that, the magnitude of the offset at high I_{probe} is larger by $\sim$0.02 than at low I_{probe} (see below). The corresponding power dependence was measured at the pump – probe delay time $t = 50$ fs. Both power-dependence measurements show a linear relationship in the log – log plot of the net parent ion signals (S) versus the I_{pump} in the pump-laser energy region of 0.3 – 1.0 μJ pulse^{-1}. The slopes of the two plots were obtained to be 1.27 ± 0.02 for the upper trace and 0.94 ± 0.02 for the lower trace, where the uncertainties represent two standard errors.

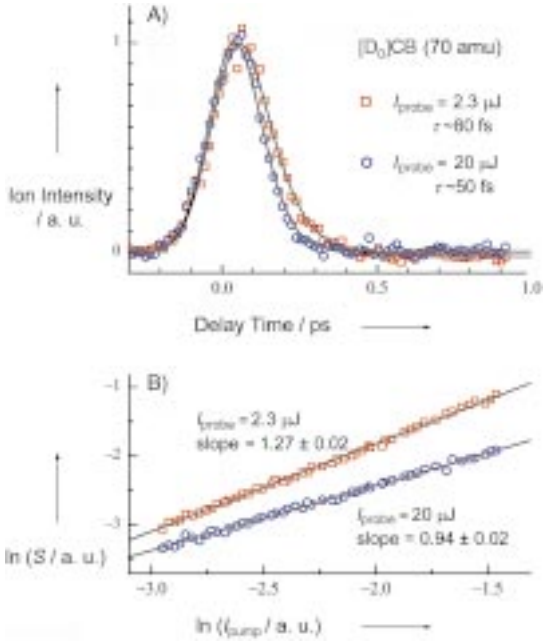

Figure 2. A) Transients of cyclobutanone at 70 amu ($I_{pump} = 0.6$ μJ pulse^{-1}) with two different probe intensities and the corresponding time constants (τ) as indicated. B) Pump-laser power dependence of cyclobutanone at 70 amu with the pump-pulse energy in the range 0.3 – 1.0 μJ. The ion signals were taken at t = 50 fs with two different probe intensities and the corresponding slopes as indicated.

Figure 3 A shows the ps transients of the fragment ions of $[D_0]$-, $[D_2]$-, and $[D_4]$CB. The ion peaks corresponding to the fragment transients were marked as stars (*) in Figure 1. The transients are

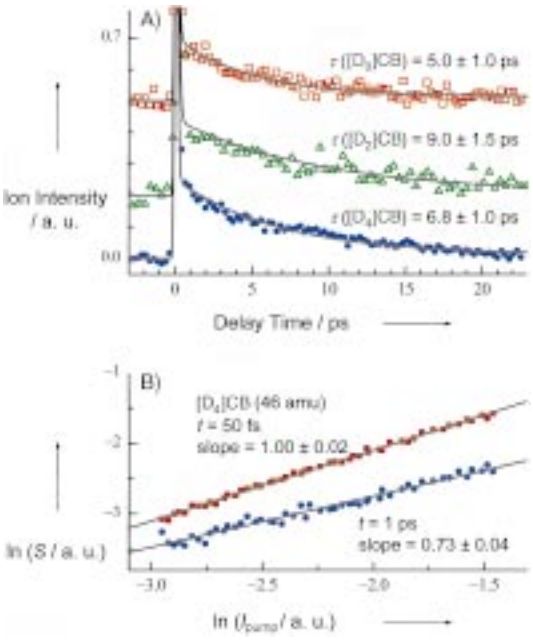

Figure 3. *A) Transients of $[D_0]$-, 3,3-$[D_2]$-, and 2,2,4,4-$[D_4]$cyclobutanone taken at the marked fragment masses (Figure 1) with the corresponding decay time constants τ as indicated. The baselines of the $[D_0]$- and $[D_2]$CB transients have been vertically shifted for clarity. B) Pump-laser power dependence of $[D_4]$CB at 46 amu with the pump-pulse energy in the range 0.3 – 1.0 μJ. The ion signals were taken at the high probe intensity (pulse energy 20 μJ) with two different delay times and the corresponding slopes as indicated.*

characterized by a fast-decay spike and a slow-decay component. The fast-decay spike has a prompt decay time constant which is similar to that of the parent. On the other hand, the slow-decay component is characterized by a single exponential decay function with the time constants of $\tau([D_0]CB) = 5.0 \pm 1.0$, $\tau([D_2]CB) = 9.0 \pm 1.5$, and $\tau([D_4]CB) = 6.8 \pm 1.0$ ps. Figure 3 B again demonstrates the pump-laser power dependence for $[D_4]$CB (46 amu) at $t = 50$ fs and 1 ps. At $t = 50$ fs, the observed slope (1.00 ± 0.02) is consistent with that of the $[D_0]$CB parent signal (0.94 ± 0.02) using the same probe intensity ($I_{probe} = 20$ μJ). At $t = 1$ ps, however, the observed slope is only 0.73 ± 0.04, which is substantially lower than that at $t = 50$ fs. Therefore, the origin of the slow-decay component is clearly different from that of the fast-decay spike in the fragment transients, and its consequence will be discussed in the later Sections.

3. Theoretical Calculations

The theoretical methods have been detailed elsewhere.[1] Briefly, the ground-state PES of CB was calculated using the DFT method. The $n \rightarrow \pi^*$ excited-state PESs, including the singlet and its triplet counterpart, were characterized using the multiconfiguration self-consistent field (MCSCF) approach and the time-dependent (TD) DFT method.[23] All of the electronic structure calculations were performed using the Gaussian software package.[24]

3.1. Ground-State Potential Energy Surface

The geometry of each species (reactant, intermediates, products, and the corresponding transition states) was fully optimized using the B3LYP hybrid functional[25, 26] with the 6-31G(d) basis set.[27] The normal-coordinate vibrational frequencies were calculated in order to determine the nature of stationary points and to include zero-point energy (ZPE) corrections for the PES. The spin-restricted method was used for all closed-shell species and the unrestricted method for open-shell species. To confirm that the TS is the correct saddle point connecting two local minima, intrinsic reaction coordinate (IRC) calculations were further performed. We have previously demonstrated that the implementation of a triple-zeta basis set in a DFT calculation may significantly improve the ground-state PES involving diradical species.[28] Therefore, further single-point energy calculations at the B3LYP/6-311G(d,p) level were carried out.

A schematic presentation of the global ground-state PES is shown in Figure 4. Selected optimized geometries of the relevant species are shown in Figure 5 and the detailed results are summarized in Table 1. Further single-point energy calculations using the 6-311G(d,p) basis set indeed substantially improve the relative energies for those originally optimized at

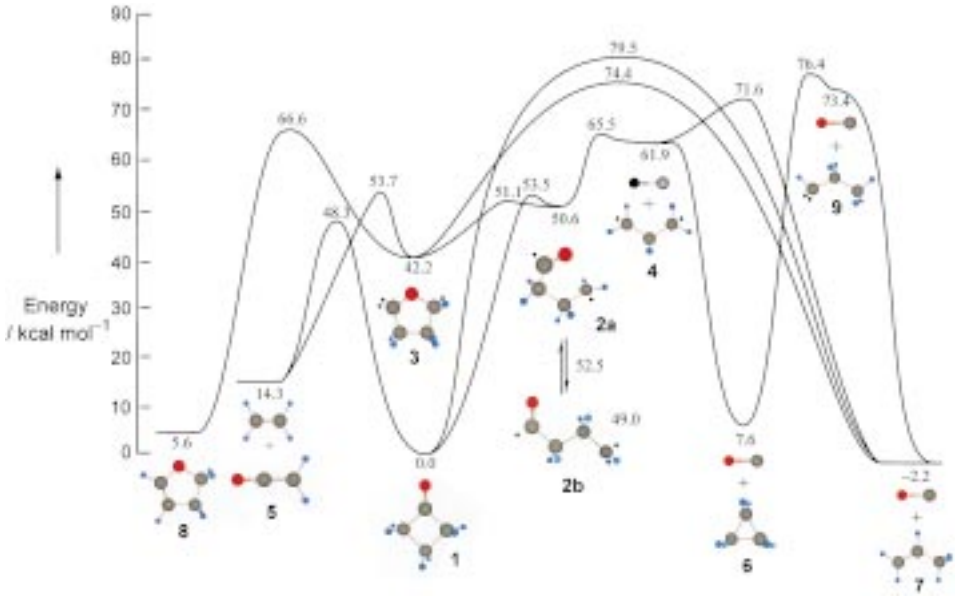

Figure 4. *Reaction coordinate diagram of cyclobutanone representing the global ground-state PES along different reaction channels. The stationary points shown in the diagram are characterized at the B3LYP/6-311G(d,p)//B3LYP/6-31G(d) level of theory with ZPE corrections. Detailed results are given in Table 1.*

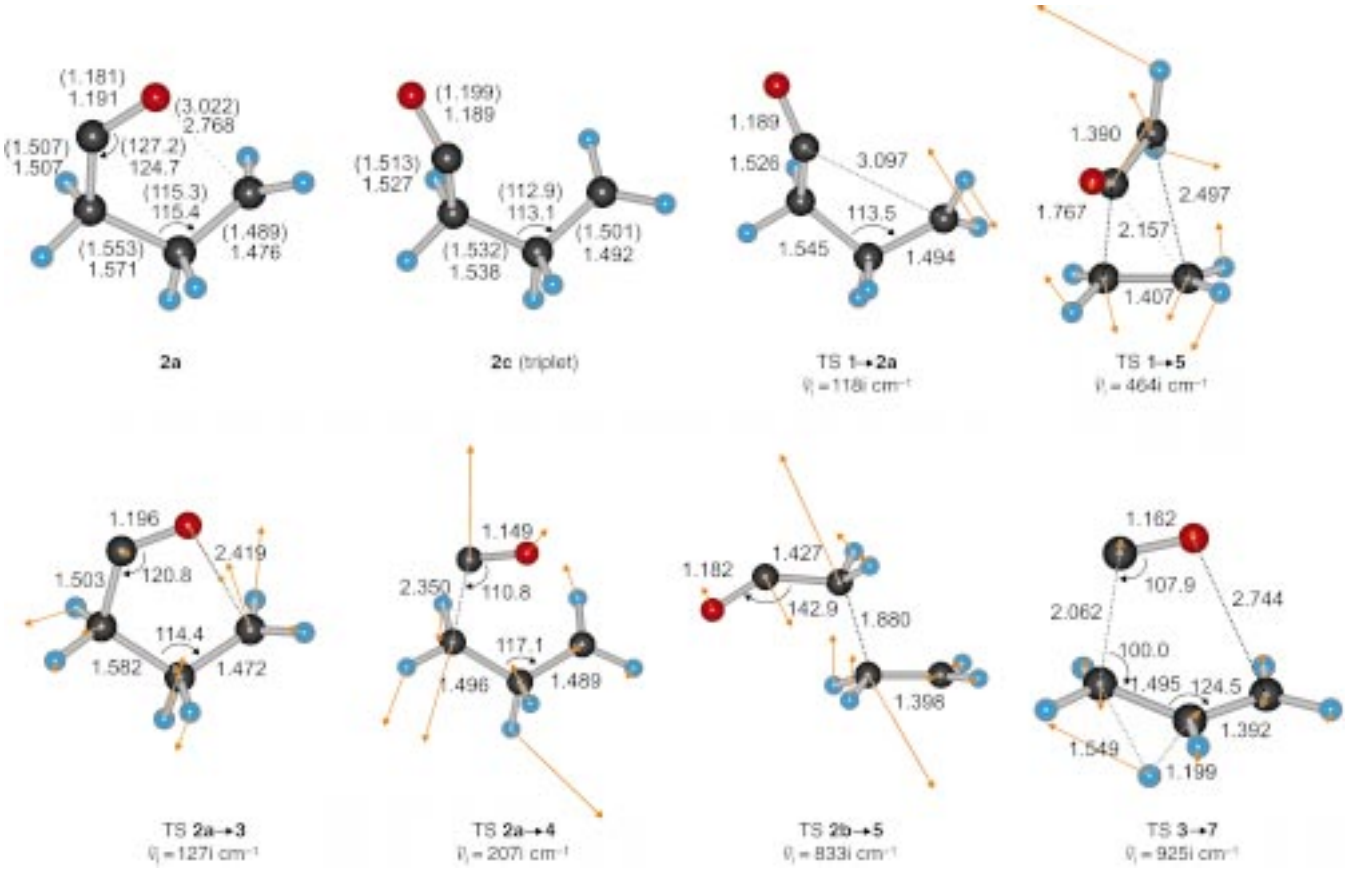

Figure 5. *Structures of selected ground-state intermediates and transition states optimized at the B3LYP/6-31G(d) level of theory with corresponding bond lengths [Å] and bond angles [°] as indicated. The values shown in parentheses are for the geometry optimized at the CASSCF(10,8)/6-31G(d) level. The vectors represent the normal-coordinate motions corresponding to the imaginary frequency of the transition states.*

Table 1. *Total energies* E *[hartree] and relative energies* ΔE *[kcal mol^{-1}] of relevant stationary points on the ground state C_4H_6O PES.*[a]

	species	E[b]	ZPE[b,c]	ν_i[b,d]	$\langle S^2 \rangle$[b]	ΔE[b,e]	ΔE[e,f]
1	Cyclobutanone	− 231.22858	57.2		0.000	0.0	0.0
2a	Butanal-1,4-diyl (C_1)	− 231.13910	54.3		0.812	53.2	50.6
2b	Butanal-1,4-diyl (C_s)	− 231.14226	54.4		0.830	51.3	49.0
2c	^{3}Butanal-1,4-diyl	− 231.13445	53.9		2.006	55.7	53.3
3	Oxacarbene	− 231.16211	57.6		0.000	42.1	42.2
4	Trimethylene + CO	− 231.10732	45.6		0.000	67.6	61.9
5	Ketene + Ethylene	− 231.18593	52.1		0.000	21.6	14.3
6	Cyclopropane + CO	− 231.20466	54.4		0.000	12.2	7.6
7	Propene + CO	− 231.21701	53.4		0.000	3.4	− 2.2
8	1,2-Didehydrofuran	− 231.22178	58.4		0.000	5.5	5.6
9	Propylidene + CO	− 231.09074	50.7		0.000	80.0	73.4
TS **1** → **2a**		− 231.13407	53.7	118i	1.006	55.7	53.3
TS **1** → **5**		− 231.14334	55.0	464i	0.000	51.2	48.3
TS **1** → **7**		− 231.09844	56.4	974i	0.000	80.8	79.5
TS **2a** → **2b**		− 231.13580	54.1	109i	0.897	55.1	52.5
TS **2a** → **3**		− 231.13882	54.6	127i	0.581	53.6	51.1
TS **2a** → **4**		− 231.10686	50.6	207i	0.966	69.8	65.5
TS **2b** → **5**		− 231.13116	53.5	833i	0.335	57.4	57.3
TS **3** → **5**		− 231.13210	54.5	487i	0.000	57.8	53.7
TS **3** → **7**		− 231.09253	52.1	925i	0.000	80.2	74.4
TS **3** → **8**		− 231.11684	55.1	1414i	0.000	68.0	66.6
TS **4** → **7**		− 231.08825	48.6	1533i	0.476	79.4	71.6
TS **6** → **9**		− 231.08676	51.3	528i	0.000	83.1	76.4
TS **7** → **9**		− 231.09004	50.0	463i	0.000	79.7	72.3

[a] The corresponding reaction coordinate diagram is shown in Figure 4. [b] B3LYP/6-31G(d). [c] Zero-point energy [kcal mol^{-1}]. [d] Imaginary frequency [cm^{-1}]. [e] With ZPE corrections. [f] B3LYP/6-311G(d,p)//B3LYP/6-31G(d).

the B3LYP/6-31G(d) level (Table 1). In particular, a reduction of 4–8 kcal mol^{-1} was obtained for the energies of the reaction paths involving the C_3 products. In fact, the reported relative energies characterized at the B3LYP/6-311G(d,p)//B3LYP/6-31G(d) level of theory for species **4**, **6**, **7**, **9**, TS **4** → **7**, TS **6** → **9**, and TS **7** → **9** are in good agreement (within 2 kcal mol^{-1}) with those calculated using high-level ab initio methods.[29, 30]

The calculated ground-state PES supports the fact that thermal decomposition of cyclobutanone **1** gives ketene and ethylene (C_2 products) as predominant final products.[31] However, decomposition of CB on the ground-state PES involves breaking of two σ bonds and formation of two π bonds. Therefore, this complex reaction may proceed via either a concerted or a stepwise pathway, which the former occurs in one single step whereas the latter takes place sequentially involving at least one intermediate. According to the Woodward–Hoffmann rules,[32] the ground-state concerted [2s+2a] cycloreversion of CB would be symmetry-allowed. However, the bond ruptures are highly asynchronous.[33, 34] The corresponding concerted TS **1** → **5** features a loose structure with the carbonyl carbon atom interacting with both carbons of the ethylene moiety. The energy barrier of the concerted TS **1** → **5** is lower by 5.2 kcal mol^{-1} than that of the first stepwise TS **1** → **2a**, therefore, this reaction is favored toward the concerted path according to our DFT predictions. The asynchronous concerted reaction mechanism is consistent with the experimental result that thermal decomposition of CB is not inhibited by radical scavengers.[31]

Even though the diradical **2a** is not likely to be produced via the stepwise pathway in a thermal reaction, it is an important intermediate involved in the photochemical process of CB through the Norrish type-I reaction mechanism. The direct ring-closure reactions from a diradical intermediate usually involve only a small energy barrier. Accordingly, the energy barriers of ring-closure processes are predicted to be 2.9 and 0.5 kcal mol^{-1} for the pathways of **2a** → **1** and **2a** → **3**, respectively. The latter reaction path is favored due to its lower energy barrier and the similarity of the conformations between the intermediate and the corresponding TS (Figure 5). By rotation around the central carbon–carbon bond, another conformation of the diradical intermediate (**2b**) can be reached through overcoming a rotational barrier of 1.9 kcal mol^{-1}. Energetically, **2b** (C_s symmetry) is more stable than **2a** (C_1 symmetry) by 1.6 kcal mol^{-1}. However, the rotational barrier between **2a** and **2b** is higher than the ring-closure barrier of **2a** → **3** (1.9 versus 0.5 kcal mol^{-1}), which may be the reason behind the observed conservation of stereochemistry in the photochemistry of substituted cyclobutanones in solution.[9]

Ketene and ethylene (**5**) were observed to be the dominant final products of the C_2 channel in the photoreaction of CB.[7] Our calculations indicate that oxacarbene **3** may be an intermediate involved in the reaction because the energy barrier of the process **2a** → **3** → **5** is lower by ~4 kcal mol^{-1} than that of the pathway (**2a** ⇔ **2b**) → **5** (Table 1). Note that the search for the direct TS of **2a** → **5** was always converged to the TS of **2a** → **3**. The evidence of a five-membered ring oxacarbene as an intermediate was also confirmed by the photochemical studies of **1** in solution, where trapping products of **3** were observed.[35]

Oxacarbene **3** is isoelectronic with 1,2-aza-cyclopentane, which is known to easily produce the trimethylene diradical through N_2 extrusion.[36] This suggests that cyclopropane and CO (C_3 products) may be produced via decarbonylation of **3**. However, the C_2 channel is energetically preferred once **3** is formed. Propene has been observed as a minor C_3 product to be produced from the photochemical process[21] via vibrationally hot cyclopropane undergoing either the **6** → **4** → **7** or **6** → **9** → **7** process, as suggested in recent theoretical work.[30] The details of the photochemical process of CB involving the first singlet excited-state PES will be discussed in the following Sections.

3.2. Excited-State Potential Energy Surfaces

The stationary points on the excited-state PESs of CB were characterized using the CASSCF method.[37, 38] In general, the active space was chosen to include two sets of CC σ and σ* orbitals, one set of CO π and π* orbitals, and two nonbonding orbitals of the oxygen atom, and ten electrons are distributed among these eight orbitals.[1] Therefore, the CASSCF(10,8)/6-31G(d) approach is capable of describing the α-CC bond-dissociation pathway as well as the higher excited states. Furthermore, based upon the linear response theory for the TDDFT calculations,[23] the vertical electronic excitation spectrum of CB (C_{2v} symmetry) was also predicted using the B3P86 hybrid functional[25, 39] and a 6-311++G(d,p) basis set at the B3LYP/6-31G(d) ground-state equilibrium geometry.

The vertical excitation energies and the oscillator strengths calculated at the TD-B3P86/6-311++G(d,p) level are illustrated in Figure 6 together with the experimental absorption spectra of the n → π* transition[19] and the higher electronic transitions[40] involving Rydberg states for comparison. The excellent agreement between the vertical transitions predicted by the TDDFT method and the experimental spectra is nicely shown.

The optimized CASSCF geometries of CB in the S_0 ground state as well as in the singlet S_1(n,π*) and triplet T_1(n,π*) excited states are shown in Figure 7, and the corresponding energies are summarized in Table 2. The molecule in the S_0 state has C_{2v} symmetry with a planar carbonyl four-membered ring structure. Constraining the C_{2v} symmetry for the molecule and optimizing its geometry in the S_1 state, a structure with the CO bond length increasing from 1.196 to 1.354 Å results. This exhibits the nature of the n → π* transition where the carbonyl moiety attempts to reduce its π-bonding character. With release of the symmetry for the $S_1(C_{2v})$ species, an optimized S_1 minimum structure with C_s symmetry was obtained. This $S_1(C_s)$ species is characterized by an out-of-plane bent structure with a CO pyramidal angle of 49.7° and a ring-puckering angle of 13.6°. Furthermore, we also found another S_1 minimum of CB with only C_1 symmetry as we have reported in the previous article on acetone.[1, 41]

At the S_1 state, the second derivatives of energy (force constants) of the Franck–Condon geometry (C_{2v}) were computed to have three negative eigenvalues corresponding to the CO

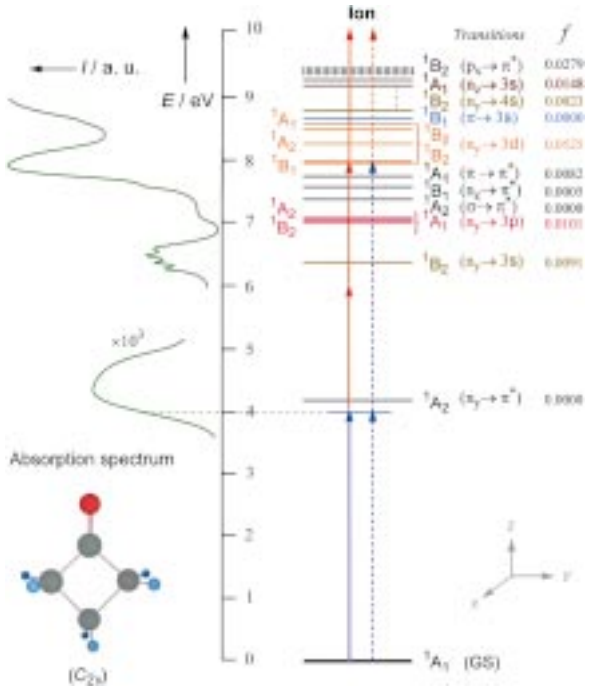

Figure 6. Two pump – probe ionization schemes proposed for the observed transient signals. The absorption spectra shown on the left side are adopted from refs. [19, 40]. The vertical transitions and the corresponding oscillator strengths (f) are predicted using the TDDFT method at the B3P86/6-311 ++ G(d,p) level of theory.

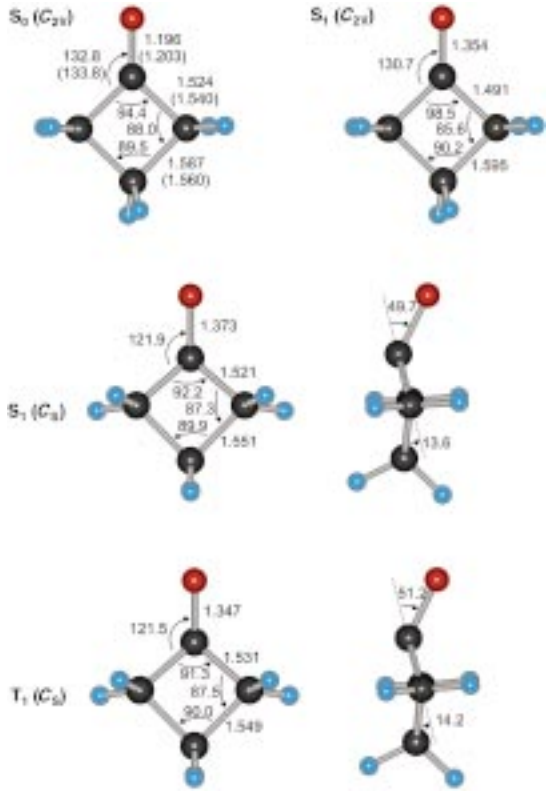

Figure 7. The structures of the $S_0(C_{2v})$, $S_1(C_{2v})$, $S_1(C_s)$, and $T_1(C_s)$ species optimized at the CASSCF(10,8)/6 – 31G(d) level of theory with corresponding bond lengths [Å] and bond angles [°] as indicated. The values shown in parentheses are for the $S_0(C_{2v})$ geometry optimized at the B3LYP/6-31G(d) level of theory. The side view and the out-of-plane bending angles for both $S_1(C_s)$ and $T_1(C_s)$ are also shown.

Table 2. *Total energies E [hartree] and relative energies ΔE [kcal mol^{-1}] of minima, transition states, and conical intersection on the S_0, S_1, and T_1 surfaces.*

species	E CASSCF[a]	ZPE[a,b]	ΔE CASSCF[a,c]	E DFT[d]	ΔE DFT[c,d]	ΔE Exp.[14]
S_0 (C_{2v})	− 229.86830	60.7	0.0	− 231.97901	0.0	0
2a	− 229.79789	58.3	41.7	− 231.88640	55.6	
2c	− 229.81272	58.2	32.3	− 231.88170	58.5	
S_1 (C_{2v})	− 229.72332	59.2	89.4	− 231.82513	94.9	
S_1 (C_s)	− 229.75001	60.3	73.7	− 231.82710	94.8	86.6
S_1 (C_1)	− 229.74901	60.1	74.2	− 231.82902	93.4	
S_1-TS	− 229.73865	58.5	79.1	− 231.82501	94.4	89 – 91
S_0/S_1 CI	− 229.75677		67.7[e]			
T_1 (C_s)	− 229.76196	60.3	66.2	− 231.85543	77.0	
T_1 (C_1)	− 229.75880	59.8	67.7	− 231.85661	75.8	
T_1-TS	− 229.75570	58.6	68.5	− 231.85529	75.4	

[a] CASSCF(10,8)/6 – 31G(d). [b] Zero-point energy [kcal mol^{-1}]. [c] With ZPE corrections. [d] TD (or U) B3P86/6-311 ++ G(d,p)//CASSCF(10,8)/6-31G(d). [e] With ZPE adopted from S_1-TS.

out-of-plane wagging (b_1), the CO in-plane wagging (b_2), and the ring-puckering (b_1) motions. Following the out-of-plane eigenvector direction downhill, with the geometry optimization constrained to C_{2v} symmetry, eventually only one negative eigenvalue was found at the optimized $S_1(C_{2v})$ structure. Therefore, this $S_1(C_{2v})$ species corresponds to a transition state (saddle point) with only one imaginary frequency corresponding to the b_1-type normal mode, namely the CO out-of-plane wagging motion. Two relevant b_1 normal-mode vectors for the $S_1(C_{2v})$ species are shown in Figure 8 A, where the vibrational frequency of the ring-puckering mode is 137 cm^{-1} and that of the CO out-of-plane wagging mode has an imaginary value of 419i cm^{-1}.

The nature of a b_1 imaginary frequency for the $S_1(C_{2v})$ species indicates that the true minimum at the S_1 state must relax the geometry by breaking the C_{2v} symmetry from moving out of the (y, z) plane but still preserving the (x, z) symmetry plane. As a result, the structure of the S_1 minimum was obtained via geometry optimization following this b_1 out-of-plane eigenvector direction of $S_1(C_{2v})$ and releasing the molecular and orbital symmetry from C_{2v} to $C_s(x, z)$. At this $S_1(C_s)$ structure, all the vibrational frequencies are real numbers (Table 3). Four relevant normal-coordinate motions of the $S_1(C_s)$ species are shown in Figure 8 B for clarity. The vibrations of the top two modes (a′) are perpendicular to the (y, z) symmetry plane and directly related to the b_1-type vibrational modes shown in Figure 8 A. On the other hand, the motions of the bottom two modes (a″) are parallel to the (y, z) symmetry plane, which may feasibly couple to the CC bond-stretching motion and eventually lead to the α-cleavage of the cyclic ketone.

Vibrational frequencies of the $S_0(C_{2v})$ and $S_1(C_s)$ species are listed in Table 3 together with the available experimental values[16, 42, 43] for comparison.[44] For the $S_1(C_s)$ frequencies, the difference between the calculated values and those assigned based on the jet-cooled fluorescence spectra[16a] is considerable (Table 3). However, fairly good results were obtained for both the ν_3 and ν_{26} modes, where the calculated values are overestimated by only $\sim$3% and $\sim$6% for the former and the latter, respectively. The comparison between theory and

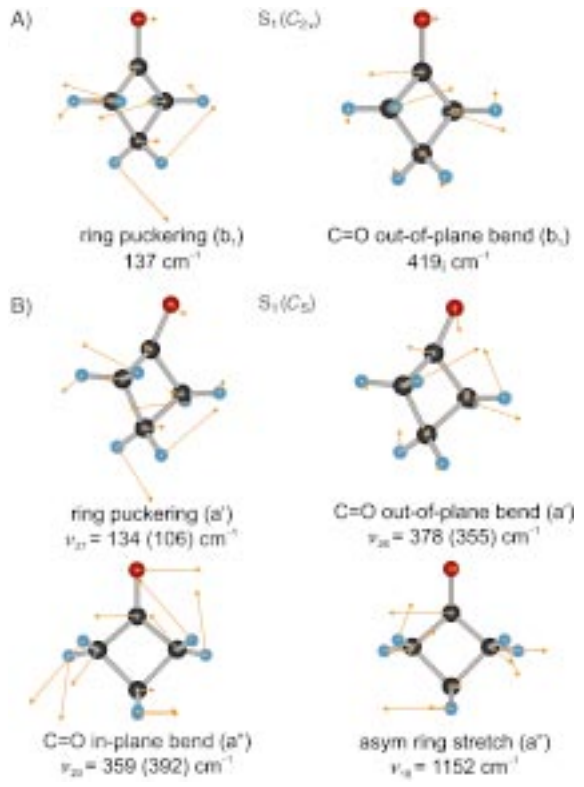

Figure 8. *A) Two b_1 normal-coordinate vectors of the $S_1(C_{2v})$ species corresponding to the ring-puckering and the CO out-of-plane wagging motions. B) Normal-coordinate vectors of the $S_1(C_s)$ species corresponding to the ring-puckering (ν_{27}), the CO out-of-plane wagging (ν_{26}), the CO in-plane wagging (ν_{20}), and the asymmetric ring-stretching (ν_{18}) motions. The frequencies shown in parentheses are the experimental values.[16a]*

experiment suggests that the ν_3 CO stretching mode may be a more appropriate assignment to the observed spectra than the other assignments based on the ν_7, ν_8, and ν_9 CC stretching modes.[16a] Furthermore, based upon the calculated force constants of [D_0]CB, we also evaluated the vibrational frequencies for both [D_2]CB and [D_4]CB. The frequency ratios that represent the isotope effect of each normal mode are listed in Table 3. The excellent agreement between theoretical predictions and experimental measurements for the values of the ν([D_4]CB)/ν([D_0]CB) ratios of the ν_3, the ν_{26}, and the ν_{27} normal modes indicates that these three vibrational motions are surely activated upon excitation. On the other hand, the poor agreement for the ν([D_4]CB)/ν([D_0]CB) ratio of the ν_{20} in-plane wagging mode (0.94 versus 0.84; Table 3) may indicate that either the spectroscopy data was misassigned or this normal mode is strongly coupled with other modes involving substantial α-CH_2 motions.

The jet-cooled fluorescence excitation spectra have unambiguously shown the vibrational progressions due to both the CO out-of-plane wagging (ν_{26}) and the ring-puckering (ν_{27}) motions.[15, 16] The former motion involves a barrier to inversion fitted to be 5.3 – 6.1 kcal mol^{-1} and the equilibrium wagging angle of 39 – 42° whereas the latter motion is essentially barrierless with the equilibrium puckering angle of ~12°. In comparison with these spectroscopy data, our $S_1(C_s)$ minimum optimized at the CASSCF(10,8)/6-31G(d) level overestimates the equilibrium wagging angle by ~10° but it is in good agreement for the ring-puckering angle. Note that attempts to locate a boatlike S_1 minimum using the same CASSCF approach was unsuccessful, so the $S_1(C_s)$ minimum has a conformation with the ring puckered into the other side of the CCC plane with respect to the CO group (a chairlike structure; Figure 7). The $S_1(C_{2v})$ species is actually a saddle point connecting both identical $S_1(C_s)$ minima on the global S_1 PES, as demonstrated in the case of acetone.[1] A topological picture regarding these two important out-of-plane vibrational motions emerges by fitting the spectral data into a two-dimensional potential energy function along the wagging and puckering coordinates.[16a]

Recent high-level ab initio calculations predicting the $S_1(n,\pi^*)$ vibronic spectra of acetone[38] have indicated that 94% of the absorption intensity from the symmetry-forbidden $^1A_1 \rightarrow {}^1A_2$ ($n \rightarrow \pi^*$) transition is borrowed from the symmetry-allowed $^1A_1 \rightarrow {}^1B_2$ ($n \rightarrow 3s$) transition through the out-of-plane normal modes with B_1 symmetry. The other 6% of the intensity is borrowed from the higher Rydberg state with B_1 symmetry through the b_2 in-plan bending motion. Based on a similar vibronic intensity-borrowing mechanism, the 94% intensity predicted in the spectra of acetone due to the b_1 vibrational modes is expected for the spectra of cyclobutanone due to the analogous CO out-of-plane wagging and the ring-puckering motions (Figure 8). Furthermore, the 6% intensity borrowed from the b_2 vibrational mode may be due to the CO in-plane wagging motion (ν_{20}) shown in Figure 8 B. These b_1- and b_2-type vibrational motions may play a key role in the observed S_1 dynamics of CB, which will be detailed in the Discussion.

The ring-opening transition state (S_1-TS) of CB was successfully located by searching for a saddle point along the α-CC bond-cleavage reaction coordinate (RC) on the S_1 surface. The symmetry of the S_1-TS species is C_1. The frequency calculation indicates that there is one (and only one) imaginary value (723i cm^{-1}) corresponding to the asymmetric CC stretching motion (bond-breaking RC). The optimized structure of S_1-TS and the normal-coordinate vector with respect to the bond-breaking RC are shown in Figure 9. Basically, the geometry of the S_1-TS species is characterized by a lengthened CC bond distance (RC = 1.862 Å) and a widely bent CCO angle (135.8°). However, the characteristic CC bond length (RC) of the S_1-TS of CB is much shorter than that of acetone (1.86 versus 2.05 Å) and other ketones,[1] to indicate a relatively early transition state feature for the S_1-TS.

As collated in Table 2, the relative CASSCF energies of $S_1(C_s)$ and S_1-TS are 73.7 and 79.1 kcal mol^{-1}, respectively, with regard to the $S_0(C_{2v})$ species. On the triplet surface, the energies of $T_1(C_s)$ and T_1-TS are 66.2 and 68.5 kcal mol^{-1}, respectively. Therefore, the energy barriers corresponding to the ring-opening process on the S_1 and the T_1 surfaces are 5.4 and 2.3 kcal mol^{-1}, respectively. Based on the TDDFT approach, the barrier height of the S_1 α-cleavage ring-opening process is dramatically reduced to 1 kcal mol^{-1} (with the energy relative to the $S_1(C_1)$ species) and the energy barrier corresponding to the T_1-TS

Table 3. *Vibrational frequencies [cm^{-1}] of the equilibrium cyclobutanone species in the S_0 and S_1 states.*

Mode	S_0 (C_{2v}) B3LYP[a]	CASSCF[b]	Exp.[42, 43]	Description	S_1 (C_s) CASSCF[b,c]	Description	$\nu([D_2]CB)/\nu([D_0]CB)$	$\nu([D_4]CB)/\nu([D_0]CB)$[c]
$\nu_1(a_1 \rightarrow a')$	3070	3240	2934	α-ν(CH)	3225	α-ν(CH)	1.000	0.729
$\nu_2(a_1 \rightarrow a')$	3097	3259	2892	β-ν(CH)	3250	β-ν(CH)	0.728	1.000
$\nu_3(a_1 \rightarrow a')$	1891	1981	1814	ν(=O)	1290 (1251)[e]	ν(C=O) + α-CH_2 wag	0.979	1.009 (0.993)
$\nu_4(a_1 \rightarrow a')$	1474	1597	1470	α-CH_2 scissor	1621	α-CH_2 scissor + β-CH_2 scissor	1.009	0.765
$\nu_5(a_1 \rightarrow a')$	1526	1635	1401	β-CH_2 scissor	1654	β-CH_2 scissor + α-CH_2 scissor	0.740	0.991
$\nu_6(a_1 \rightarrow a')$	1258	1369	1291	α-CH_2 wag	1416	α-CH_2 wag + ν(C=O)	0.998	0.845
$\nu_7(a_1 \rightarrow a')$	975	970	1017	ν(C-C)	1017 (714)	ν(C-C)	0.975	0.891 (0.915)
$\nu_8(a_1 \rightarrow a')$	841	887	848	ν(C-C)	951 (679)	ν(C-C)	0.962	0.879 (0.922)
$\nu_9(a_1 \rightarrow a')$	674	715	667	ν(C-C)	659 (539)	ν(C-C)	1.075	0.945 (0.967)
$\nu_{10}(a_2 \rightarrow a'')$	3118	3291	2979	α-ν(CH)	3281	α-ν(CH)	1.000	0.742
$\nu_{11}(a_2 \rightarrow a'')$	1236	1303	1196	β-CH_2 torsion	1376	β-CH_2 torsion	0.728	0.941
$\nu_{12}(a_2 \rightarrow a'')$	959	1037	909	α-CH_2 torsion	1104	α-CH_2 torsion	0.085	0.728
$\nu_{13}(a_2 \rightarrow a'')$	639	728	(1163)[d]	α-CH_2 rock	842	α-CH_2 rock + β-CH_2 torsion	0.891	0.798
$\nu_{14}(b_2 \rightarrow a'')$	3066	3238	2934	α-ν(CH)	3221	α-ν(CH)	1.000	0.728
$\nu_{15}(b_2 \rightarrow a'')$	1459	1591	1401	α-CH_2 scissor	1618	α-CH_2 scissor	1.000	0.750
$\nu_{16}(b_2 \rightarrow a'')$	1287	1385	133	β-CH_2 wag	1414	β-CH_2 wag + α-CH_2 wag	0.799	0.995
$\nu_{17}(b_2 \rightarrow a'')$	1206	1314	1243	α-CH_2 wag	1329	α-CH_2 wag + β-CH_2 wag	1.027	0.808
$\nu_{18}(b_2 \rightarrow a'')$	1092	1227	1125	ν(C-C)	1152	ν(C-C_α)	1.070	1.015
$\nu_{19}(b_2 \rightarrow a'')$	933	906	957	ν(C-C)	1004	ν(C_α-C_β)	0.872	0.910
$\nu_{20}(b_2 \rightarrow a'')$	456	493	457	δ(C=O) in plane	359 (392)	δ(C=O) in plane	0.992	0.941 (0.837)
$\nu_{21}(b_1 \rightarrow a')$	3112	3284	3005	α-ν(CH)	3277	α-ν(CH)	1.001	0.744
$\nu_{22}(b_1 \rightarrow a')$	3147	3313	2979	β-ν(CH)	3305	β-ν(CH)	0.743	0.998
$\nu_{23}(b_1 \rightarrow a')$	1233	1301	1209	α-CH_2 torsion	1341	α-CH_2 torsion + β-CH_2 rock	0.992	0.859
$\nu_{24}(b_1 \rightarrow a')$	1109	1183	1073	α-CH_2 rock	1153	α-CH_2 rock	0.979	0.873
$\nu_{25}(b_1 \rightarrow a')$	747	776	734	β-CH_2 rock	806	β-CH_2 rock + α-CH_2 torsion	0.770	0.868
$\nu_{26}(b_1 \rightarrow a')$	402	424	395	δ(C=O) in plane	378 (355)	δ(C=O) in plane	0.992	0.882 (0.882)
$\nu_{27}(b_1 \rightarrow a')$	28	45	36	ring puckering	134 (106)	ring puckering	0.914	0.907 (0.896)

[a] B3LYP/6-31G(d). [b] CASSCF(10,8)/6-31G(d). [c] Experimental values[16] in parentheses. [d] Uncertain mode. [e] Alternative assignment in ref. [16].

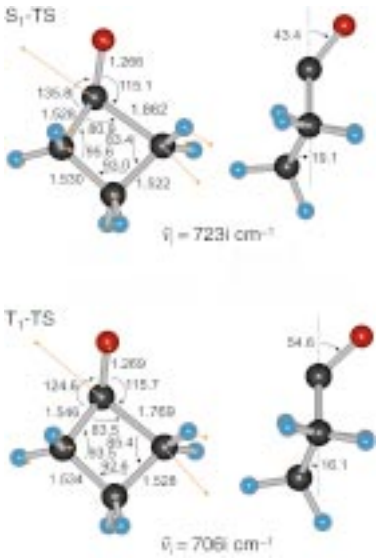

Figure 9. *The structures of the S_1-TS and T_1-TS species optimized at the CASSCF(10,8)/6-31G(d) level of theory with corresponding bond lengths [Å] and bond angles [°] as indicated. The side view and the out-of-plane bending angles are also shown. The vectors represent the normal-coordinate motions corresponding to the imaginary frequency.*

essentially disappears. In fact, the calculated energy barriers (S_1-TS and T_1-TS) of CB are significantly lower than those of acetone and other aliphatic ketones,[1] which indicates the relevance of the ring strain in the four-membered cyclic skeleton affecting the α-cleavage PES of CB.[45]

We have performed mass-weighted IRC calculations for the S_1-TS so that the reaction path on the S_1 surface can be followed according to the direction of the normal-coordinate vector shown in Figure 9. On one side, the S_1 minimum is approached by following the "forward" direction of the IRC path. On the other side, we did encounter the difficulties of optimizing the CASSCF orbitals when following the "reverse" direction of the IRC path at IRC < -0.07 bohr amu$^{1/2}$. Following the reverse IRC path from the S_1-TS to the last point where the CASSCF optimization is successful, the geometry has changed mostly by the increase of the α-CC bond distance (from 1.862 to 2.006 Å) and the expansion of the CCO bending angle (from 135.8° to 139.8°). Furthermore, the CASSCF energy has been lowered from -229.7387 to -229.7431 hartree together with the S_0/S_1 energy gap substantially shrunk from 0.0587 to 0.0265 hartree. Therefore, the S_1 state-specific CASSCF optimization failure after IRC < -0.07 bohr amu$^{1/2}$ is the result of the breakdown of the Born–Oppenheimer approximation in the adiabatic S_1 PES when the S_0 surface rapidly approaches the S_1 surface along the bond-breaking RC. This implies that, further following the reverse IRC path on the S_1 surface, one needs to consider the sharply increased interaction between the S_1 and S_0 surfaces and the state-average CASSCF method must be implemented to search for the expected S_0/S_1 conical intersection (Figure 10) at the lowermost surface crossing point.[46]

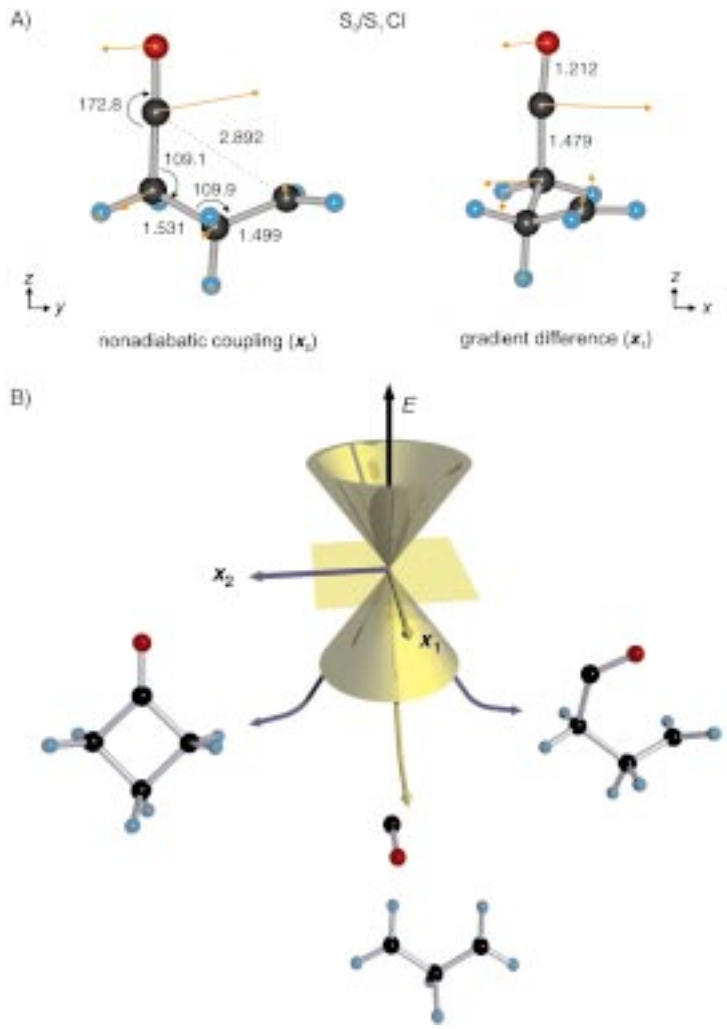

Figure 10. A) The structures of the S_0/S_1 CI optimized at the CASSCF(10,8)/6-31G(d) level of theory with corresponding bond lengths [Å] and bond angles [°] as indicated. The nonadiabatic coupling ($\mathbf{x}_2$) and the gradient difference ($\mathbf{x}_1$) vectors are shown with the skeleton of the molecule parallel to the (y, z) and (x, z) plane for the former and the latter, respectively. B) Ground-state branching paths resulting from the S_0/S_1 CI: Following the nonadiabatic coupling vector $\mathbf{x}_2$, either the hot parent molecule (left) or the acyl diradical (right) is produced; following the gradient difference vector $\mathbf{x}_1$ either the trimethylene and CO (middle) or hot cyclopropane and CO (not shown) are formed.

3.3. The S_0/S_1 Conical Intersection

The conical intersection is known to be a "photochemical funnel" in many nonadiabatic photoreactions.[5, 6, 47–51] Since the process of funneling through a CI is very efficient, the nonradiative decay from the upper to the lower intersecting state usually occurs within a single vibrational period.[50, 51] Furthermore, the structural information of a CI may provide significant insight into the mechanism of photoproduct formation on the global ground-state PES.[47–52, 55, 56] The single crossing point of a double cone formed by two intersecting surfaces is schematically shown in Figure 10B, where the bifurcated character of the conical intersection along the ($\boldsymbol{x}_1$, $\boldsymbol{x}_2$) branching space is also indicated.

Starting from the last successful point of the reverse IRC path on the S_1 surface of CB, the lowest energy point of the surface crossing seam (S_0/S_1 CI) was obtained by minimizing the energy in the $n-2$ (=25) dimensional intersection space and preserving the degeneracy of the two-dimensional branching space. Under a tight convergence criterion for both gradient and displacement, the total energy of the S_0/S_1 CI was optimized to be -229.75677 hartree with the S_0/S_1 energy gap less than 10^{-6} hartree. The relative energy of the CI is estimated to be 70 and 26 kcal mol^{-1} with regard to S_0 and the singlet diradical (**2a**), respectively, without ZPE corrections. The optimized structure and the corresponding $\boldsymbol{x}_1$ and $\boldsymbol{x}_2$ vectors are shown in Figure 10A.

There are three important points regarding the structure and the two vectors of the S_0/S_1 CI worthy of emphasis in the following. First, the main structural feature of this S_0/S_1 CI is the almost linear CCO bending angle (172.8°). This theoretical finding is consistent with the early state-correlation picture of the Salem diagram, which states that the α-cleavage of the S_1 CB is favored by forming a linear acyl diradical intermediate with topicity equal to three (tritopic).[6, 13] Second, the linear character of the CCO bending angle is very significant because the nonradiative dynamics on the S_1 surface must be related to the vibrational motions involving the substantial change of the angle. Following the minimum-energy pathway of the S_1 surface, our calculations indicate that the CCO bending angle is originally 132.8° in the Franck–Condon region and it reduces to 121.9° in the $S_1(C_s)$ minimum geometry. However, the angle expands to 135.8° at the S_1-TS structure and eventually becomes almost linear at the S_0/S_1 CI region. This structural feature along the S_1 α-cleavage PES of CB is very similar to that of acetone.[1] Further discussion of this bending motion affecting the nonradiative dynamics of the S_1 state will be addressed in the next Section.

Third, the gradient difference and nonadiabatic coupling vectors give an indication of the possible reaction paths to be followed on the ground-state surface after funneling through the CI. As illustrated in Figure 10B, the nonadiabatic coupling vector $\boldsymbol{x}_2$ corresponds to a CCO bending motion parallel to the original molecular symmetry plane (*y*, *z*), which could lead to formation of either a hot parent cyclobutanone molecule (**1***) or the α-cleavage diradical (**2a**) and eventually give the C_2 products. On the other hand, the gradient difference vector $\boldsymbol{x}_1$ corresponds to a CCO bending motion parallel to the (*x*, *z*) plane, which could lead to the reaction path of decarbonylation and finally give the C_3 products. This important feature indicates that upon excitation to the $S_1(n,\pi^*)$ state above the dissociation threshold, both C_2 and C_3 products in the S_0 state can be directly populated from the S_1 state via the guidance of two different branching vectors of the S_0/S_1 CI. Furthermore, not only the vibrationally hot ground-state molecule (**1***) is the source of the C_2 products but also the singlet diradical intermediate (**2a**) can be produced to give ketene and C_2H_4 (C_2 products) through the S_0/S_1 CI.

The significance of the S_0/S_1 CI in relation to the observed product-branching (C_3:C_2) ratio[14] is described in the following. Based on the results of singlet/triplet benzene sensitization of

CB,[14a] it was proposed that the precursor of the C_3 products is the lowest triplet state (T_1) and the C_2 products originate from the S_1 state. Therefore, the measured C_3:C_2 ratio was assumed to correspond to the nonradiative decay rate of the $S_1 \rightarrow T_1$ ISC process over that of $S_1 \rightarrow S_0$ internal conversion. However, our calculations indicate that there is a possible reaction pathway on the singlet surface of CB to give the C_3 products via the S_0/S_1 CI at the excitation energy above the dissociation threshold. Thus, the early assumption to account for the measured C_3:C_2 ratio is *not valid*. Note that the $S_1 \rightarrow T_1$ ISC process (in $\sim$5 ns) is too slow to compete with the predissociation channel (in $\sim$5 ps) when the excitation energy is higher than the S_1 α-cleavage barrier. According to our CI picture, the observed C_3:C_2 ratio of $\sim$0.5 above the dissociation threshold[14f] suggests that the possibility of following the $\boldsymbol{x_2}$ branching path to give the C_2 products is greater by a factor of two than that following the $\boldsymbol{x_1}$ branching path to give the C_3 products. The value of the C_3:C_2 ratio increases gradually from $\sim$0.4 at $\lambda_{ex} = 313$ nm to $\sim$0.8 at $\lambda_{ex} = 248$ nm, which indicates that the $\boldsymbol{x_1}$ branching path becomes progressively more important with increasing excitation energy above the threshold. Moreover, excitation to the S_1 state with different vibronic symmetry will also affect the observed C_3:C_2 ratio. It was found that the C_3:C_2 ratios are somewhat higher for excitation of the molecule to the B_1 levels than those to the totally symmetric levels[14f] thereby indicating that the vibronic coupling with B_1 symmetry favors the reaction path leading to the C_3 products. This is consistent with the nature of the branching vectors of the CI, since the gradient difference vector $\boldsymbol{x_1}$ corresponds to formation of the C_3 products via the "out-of-plane" bending motions with B_1 symmetry. Thus, a higher C_3:C_2 ratio is expected for excitation to the vibrational levels with B_1 symmetry.

Finally, the observed $\sim$85% of the total CO yield with a rotational temperature of $\sim$3000 K by 193 nm photodissociation of CB (S_2) indicates that the hot rotating CO molecule may be produced via the $\boldsymbol{x_1}$ branching path of the S_0/S_1CI (Figure 10B) after the initial $S_2 \rightarrow S_1$ internal conversion.[17]

3.4. Reaction Mechanism

According to our theoretical findings, a mechanism is presented in Scheme 1 to rationalize the observed photochemical behavior of CB upon excitation to the S_1 state above the dissociation threshold. Early photochemical quenching experiments of CB above the dissociation threshold show that the pressure-unquenchable C_3 and C_2 product yields are $\sim$0.3 and $\leq$0.1, respectively, and that the pressure-quenchable C_2 product yield

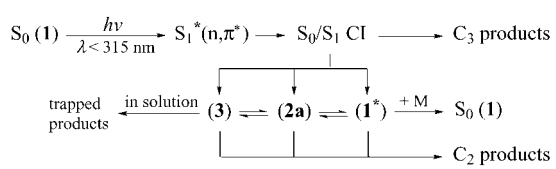

Scheme 1. *Photochemistry of cyclobutanone in the S_1 state above the α-cleavage threshold.*

is in the range of 0.6 – 0.7.[14] In the liquid phase, the vibrationally hot S_0 molecule (S_0^*) will be effectively quenched. The considerable product yield of C_2H_4 ($\sim$10%) produced in solution indicates that the S_0^* is not the only precursor of the C_2 products. This has confirmed the mechanism with the S_0/S_1 CI feature for that the unquenchable product (C_2H_4) can be produced directly by following the reaction path: $S_1^* \rightarrow$CI $\rightarrow$(**2a**) $\rightarrow C_2$ products. Furthermore, substantial amounts of the trapped products were observed in a methanol solution[14c] due to the insertion reaction of oxacarbene **3** via the reaction path: $S_1^* \rightarrow$CI $\rightarrow$(**3**) $\rightarrow$ trapped products. Note that this reaction path may be reached directly without involving **2a** due to the similar geometry between **2a** and TS **2a** $\rightarrow$**3**.

For excitation energies below the dissociation threshold, an early laser-photolysis study[14f] shows that the C_3 and C_2 product yields are 88% and 12%, respectively. It was recognized that the C_3 products are produced exclusively from the T_1 state after the $S_1 \rightarrow T_1$ ISC process. Since the C_3:C_2 ratio ($\sim$7:1) is invariant with a change in the total pressure,[14f] it is very unlikely that the C_2 products originated from a hot S_0 molecule via the initially proposed $S_1 \rightarrow S_0^* \rightarrow C_2$ products process. Rather, the $\sim$10% unquenchable C_2 products must come from singlet **2a** [^{1}(**2a**)] via an ISC process. A reaction mechanism is thus shown in Scheme 2 to clarify the observed photochemical behavior of CB upon excitation to the S_1 state below the dissociation threshold. Note that the observed 88% of the total branching may result from the reaction path of $S_1 \rightarrow T_1 \rightarrow {}^3$(**2c**) $\rightarrow {}^3$(**4**) $\rightarrow {}^1$(**4**) $\rightarrow C_3$ products, while the other 12% of the total branching should be due to the process $S_1 \rightarrow T_1 \rightarrow {}^3$(**2c**) $\rightarrow {}^1$(**2a**) $\rightarrow$ C_2 products.

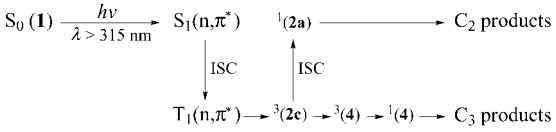

Scheme 2. *Photochemistry of cyclobutanone in the S_1 state below the α-cleavage threshold.*

Since the $S_1 \rightarrow T_1$ ISC process occurs on the nanosecond time scale ($\sim$5 ns),[14e] it cannot compete with the much faster direct-dissociation channel above the S_1 α-bond-breaking threshold. The S_1 α-cleavage dynamics of CB will be discussed in the following Section.

4. Discussion

Figure 6 illustrates the pump – probe schemes based on our experimental wavelengths ($\lambda_{ex} = 307$ nm; $\lambda_{probe} = 615$ nm) for two ionization processes that may contribute to the observed transient signals. The solid arrows describe the one-pump-photon excitation followed by three-probe-photon ionization process, so it is classified to a (1+3)-ionization scheme. The dashed arrows represent the two-pump-photon excitation plus one-probe-photon ionization process, so it belongs to a (2+1)-ionization scheme. Accordingly, the ion signals, which can be

observed due to the one-photon excitation process, would require absorbing at least three probe photons, but those due to the two-photon excitation process would require only absorbing one extra probe photon. As a result, at very low probe intensities it is most favorable to follow only the (2+1)-ionization scheme for obtaining the ion signals due to the two-photon excitation process. On the other hand, the observed transient at relatively high probe intensities may involve the ion signals resulting from many different ionization processes, such as (2+p) and (1+q) schemes, where $p = 1, 2, 3,\ldots$ and $q = 3, 4, 5,\ldots$. Note that the time scale of the observed dynamics resulting from the one-photon excitation process may be distinguishable from that of the two-photon excitation process because different photochemical processes could be involved in the different excited states. Therefore, observation of the dynamics from different excitation processes can be achieved by using different pump and probe intensities, as demonstrated in our power-dependence measurements discussed below.

4.1. Power Dependence and the Parent Transients

Figure 2A showed the transients taken under our two extreme I_{probe} conditions, where the apparent discrepancy of the transients can be rationalized due to the two different excitation processes, as mentioned above. Both transients were obtained using the same pump intensity so the initial populations in the excited states are prepared in the same way via excitation through either a one-photon or a two-photon process. However, the ionization preference of each excitation process can be determined by using different probe intensities to produce the ion signals through the aforementioned different ionization schemes. Therefore, the transient arising mainly from the (2+1)-ionization process can be obtained at our very weak probe intensity condition ($I_{probe} = 2.3$ μJ) with a fitted time constant of 80 fs. On the other hand, the transient taken at our very strong probe intensity condition ($I_{probe} = 20$ μJ) has evidently a shorter time constant ($\sim$50 fs) than that obtained at the very low I_{probe} intensity. Because the transient at high I_{probe} actually composes of the ion signals arising from both the one-photon and the two-photon excitation processes, an ultrafast-decay component ($\tau <$ 50 fs) must be involved in the transient due to the (1+q)-ionization processes increased by the intense probe laser pulse.

Our pump-laser power-dependence measurements confirm the above real-time observations with the proposed two different excitation processes. In the case of a fixed probe intensity, the slope of the pump-laser power dependence should represent the number of photons absorbed upon excitation. We have observed a value of 1.27 ± 0.02 for $I_{probe} = 2.3$ μJ and 0.94 ± 0.02 for $I_{probe} = 20$ μJ. The consequence of these observations may be summarized in the following by three major points. First, the very different slopes observed at these two extreme I_{probe} conditions confirm that there are indeed two different excitation processes involved, which can be differentiated unambiguously by ionization using very weak and strong probe intensities. Second, at the very low probe intensity the observed slope ($= 1.27$) is greater than unity, which confirms that the parent transient taken under such conditions is dominated by a two-photon *rather than* a one-photon excitation process. The deviation from what might have been anticipated for a pure two-photon process (a slope of exactly two) is the result from the fact that the two-photon excitation involves a resonant intermediate state (namely, the first $^1A_2$ excited state), as schematically shown in Figure 6. Third, at the high probe intensity the observed slope ($= 0.94$) is substantially lower than that at very low probe intensity. This observation again confirms the mixed ion-signals feature of the transient with significant involvement of the one-photon excitation process at very intense I_{probe} conditions.

Now let us focus on the special feature of the parent transients at longer delay times when the fast-decay component has declined to a background level (Figure 2A). First, there shows a very small negative background component ($\sim -2\%$) at $t > \sim 600$ fs in the transient of $I_{probe} = 2.3$ μJ. The baseline of the transient is defined as the zero-signal level at a negative pump–probe delay time when the probe pulse is ahead of the pump pulse and both pulses do not overlap with each other. Therefore, the small negative background signal at $t > \sim 600$ fs, shown in the transient of $I_{probe} = 2.3$ μJ, is due to the fragmentation of the pump-alone background ion signal induced by the delayed probe pulse. Note that the pump-alone background signal arises from a direct multiphoton ionization process involving at least three pump photons with $I_{pump} = 0.6$ μJ while the probe-alone background signal is negligible with $I_{probe} = 2.3$ μJ. Second, despite of the possible depletion of the pump-alone background ion signal at $t > \sim 600$ fs at very intense probe intensities ($I_{probe} =$ 20 μJ), a somewhat positive (instead of still more negative) background offset component was observed. This subtle background offset difference at $t > \sim 600$ fs suggests that there may exist of another transient component with a much slower decay time constant resulting from only the one-photon excitation process, which will be discussed in the following Section.

4.2. Power Dependence and the Fragment Transients

For the transients of the fragment mass at the intense I_{probe} condition, not only the parentlike fast-decay component but also the slow-decay component is pronounced (Figure 3A). Note that the slow-decay component is hardly seen in the parent transients but it becomes much more evident in the fragment transients. This indicates that ionization of the S_1 species using an intense probe pulse should efficiently lead to fragmentation in the ionic channel and give the corresponding ion signal in the fragment mass as observed in the case of acetone.[1]

This ion fragmentation mechanism is further supported by the power dependence of the fragment signals (46 amu of $[D_4]$CB, Figure 3B) measured at different delay times using the high probe intensity ($I_{probe} = 20$ μJ). The slope measured at $t = 50$ fs (corresponding to the fast-decay component) is clearly higher than that measured at $t = 1$ ps (corresponding to the slow-decay component). The slope of the fast-decay component measured at the fragment mass is similar to that measured at the parent mass (1.00 versus 0.94) at the same I_{probe} condition, which indicates that the huge spikes arising from the fast-decay

components in the fragment transients originate from the fragmentation of the parent ions. On the other hand, the observed slope at $t = 1$ ps is much lower than at 50 fs (0.73 versus 1.00), which implies that the ion signals corresponding to the slow-decay components are due to only the one-photon excitation process. Therefore, the S_1 dynamics of CB can now be isolated and studied at longer delay times when the ion signal due to the two-photon excitation process has completely disappeared. The observed partial slope value (0.73), instead of unity for the one-photon process, indicates that the power-dependence measurements were carried out at the pump-power saturation region.[53]

4.3. Fast and Slow S_1 Dynamics

The above experimental findings indicate several important points regarding the dynamic behavior of the cyclobutanone upon one-photon excitation to the S_1 state with a total excitation energy of 93 kcal mol^{-1}. First, the observed fast-decay and the slow-decay components indicate that there must be two different dynamic processes involved in the S_1 α-cleavage of CB at our excitation wavelength. Second, the fast-decay component has a pulse-limited time constant ($\tau < 50$ fs) corresponding to a very efficient dephasing process upon initial excitation. Third, the slow-decay component describes a subsequent motion with a time constant of 5 ps, to suggest that it is in nature a relatively slow dynamic process rather than a prompt bond dissociation. Finally, the dynamics of the slow-decay motion shows a prominent isotope effect for both [D_2]CB and [D_4]CB, and suggests that the corresponding dynamic process must involve certain vibrational motions relevant to the observed dynamics. A dynamic picture for the above observations is shown in Figure 11. Briefly, the less-than-50 fs dephasing process can be rationalized as an initial wave packet moving rapidly from the Franck–Condon to the S_1 equilibrium region. The observed 5 ps decay process implies the multidimensional nature of the PES upon further propagation of the wave packet along the bond-breaking RC towards the final products.

Our theoretical calculations indicate two relevant features for the dynamics of the ultrafast dephasing process. First, on account of the strong antibonding character of the CO moiety upon excitation to the $S_1(n,\pi^*)$ state, the CO bond length should stretch substantially due to the repulsive nature of the surface along the CO distance. The optimized S_1 geometry constrained to C_{2v} symmetry confirms that the CO bond length indeed increases from 1.20 to 1.35 Å. Second, because absorption to the first excited state of CB is an orbital-symmetry (or dipole moment) forbidden transition ($A_2 \leftarrow A_1$), an intensity-borrowing mechanism from the higher excited states must be applied through the appropriate vibronic coupling process.[15, 38] Based on the first-order approximation, the intensity borrowed from the next symmetry-allowed state with B_2 symmetry (Figure 6) would require the symmetry of the corresponding vibrational motion (Q) to satisfy the totally symmetric matrix element $\langle A_2 | Q | B_2 \rangle$ criterion. Therefore, Q should belong to a b_1 vibrational mode. Our normal-coordinate frequency calculation based on the optimized $S_1(C_{2v})$ structure further confirms that this b_1 vibrational motion corresponds to a CO out-of-plane wagging mode with an imaginary frequency of 419i cm^{-1} (Figure 8 A). This CO out-of-plane wagging motion has been understood as a common active mode to form a pyramidal $S_1(n,\pi^*)$ minimum for all carbonyl-containing moieties, such as in formaldehyde.[9, 10] Therefore, the geometry of the initially excited CB must be significantly distorted out of the (y, z) symmetry plane through this CO out-of-plane wagging (inversion or pyramidalization) motion activated upon excitation. On the S_1 surface, the typical vibrational period of the CO stretching is ~ 30 fs ($\nu_3 \sim 1250$ cm^{-1}) and that of the CO out-of-plane wagging motion is ~ 90 fs ($\nu_{26} \sim 350$ cm^{-1}). Therefore, our real-time observation of the initial dephasing process can be understood in terms of an ultrafast nuclear motion involving both CO stretching and CO out-of-plane wagging vibrations from the Franck–Condon region to the bent S_1 minimum area in less than a bending vibrational period ($\tau < 50$ fs).

As discussed in the previous Section, two active vibrational modes of CB have been observed in the gas-phase absorption spectrum[18] as well as in the excitation fluorescence spectrum[15, 16] and were unambiguously assigned to be the CO out-

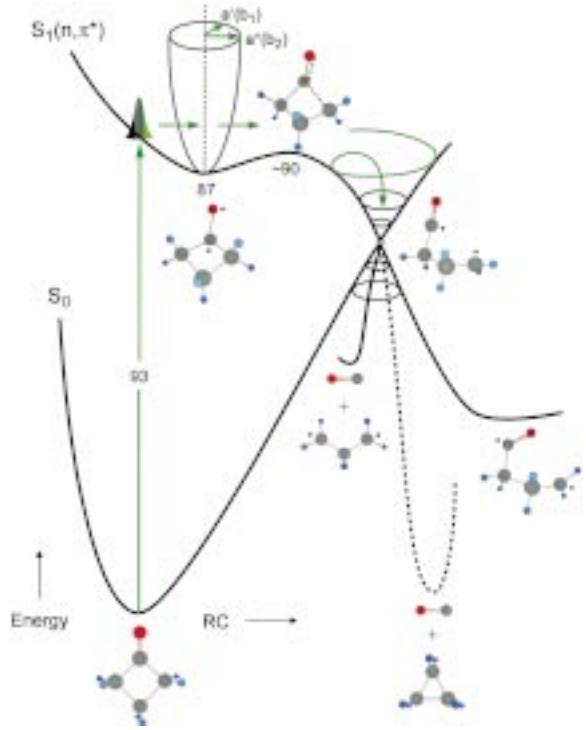

Figure 11. *A schematic reaction coordinate (RC) diagram representing the nonadiabatic process of the Norrish type-I reaction of cyclobutanone along the α-cleavage RC from the $S_1(n,\pi^*)$ minimum-energy pathway down to the global S_0 hypersurface via a pivotal conical intersection (S_0/S_1 CI). The wave packet is prepared upon excitation ($\lambda_{ex} = 307$ nm) to the S_1 state and rapidly propagating to the S_1 local minimum region. The multidimensional feature of the S_1 surface is represented by a semiellipsoid column with the arrows representing the direction of the vibrational motions: The a″(b_2) normal modes are parallel to the α-bond-breaking RC, while the a′(b_1) modes are perpendicular to the RC. The curved arrow represents a trajectory along the bond-breaking RC on the S_1 surface finding the pathway from the transition state to the conical intersection. The ground-state reaction paths reached by funneling through the S_0/S_1 CI are also shown. The numbers are relative energies [kcal mol^{-1}] with respect to the S_0 minimum.*

of-plane wagging and the ring-puckering motions. These two vibrational modes as well as the other two modes relevant to the S_1 dynamics of CB are represented as normal-coordinate vectors shown in Figure 8B based on our frequency calculations at the optimized $S_1(C_s)$ geometry. Note that both ring-puckering (ν_{27}) and CO out-of-plane wagging (ν_{26}) motions are feasibly activated upon excitation because they have the same B_1 symmetry.[16a] The other two in-plane motions (with B_2 symmetry), the CO in-plane wag (ν_{20}) and the ring asymmetric stretch (ν_{18}), are important normal modes to be considered because they couple directly to the bond-dissociation RC. Both CO in-plane wagging and asymmetric ring-stretching motions should have low activation probability upon excitation to the S_1 state according to recent studies of jet-cooled fluorescence excitation spectrum analyses of CB[15, 16] and the ab initio vibronic spectrum calculations of acetone.[38] Therefore, the dynamics corresponding to the α-cleavage of CB on the S_1 surface must involve the relevant vibrational coupling process so that the excess internal energy can be transferred from the initially activated vibrational modes into the other relevant, but originally inactive, vibrational modes through the intramolecular vibrational energy redistribution (IVR) process.

According to the early study of Hemminger and Lee,[14e] the S_1 fluorescence emission of CB was measured to have an almost constant lifetime ($\tau_S = 4.5$ ns) at $\lambda_{ex} > 316$ nm, but the emission dramatically disappears at $\lambda_{ex} < 310$ nm ($\Phi_F < 4 \times 10^{-6}$). The sharp decrease in the lifetime of the S_1 state was attributed to the onset of a new nonradiative process, namely a predissociation channel that dominates the S_1 dynamics of CB at $\lambda_{ex} <$ 310 nm. The origin of the S_1 state of CB has been carefully measured to be 30 292 cm^{-1} (330.1 nm).[16] Assuming that the predissociation threshold on the S_1 surface is about 316 nm, the energy barrier of the S_1 state along the predissociation pathway is estimated to be 1350 cm^{-1} ($\sim$4 kcal mol^{-1}). On the other hand, Tang and Lee observed rapid decrease of the C_3:C_2 ratio with increasing excitation energy at the wavelength region 335–315 nm and suggested that the energy barrier of the S_1 predissociation channel can be as low as 700 cm^{-1} ($\sim$2 kcal mol^{-1}).[14f] Our excitation energy is 93 kcal mol^{-1} ($\lambda_{ex} =$ 307 nm), so the available excess vibrational energy in our study ($E_{vib} \sim 6$ kcal mol^{-1}) is surely sufficient to surmount the predissociation energy barrier. Furthermore, the observed 5.0 ps decay time is in excellent agreement with the extrapolated S_1 lifetime of CB at the same excitation energy (that is, $\tau_S \sim 5$ ps at $E_{vib} =$ 2100 cm^{-1} or 6 kcal mol^{-1}).[14e]

Because the direct bond-breaking process is on the time scale of 100 fs,[54] the observed 5.0 ps S_1 dynamics for CB must be due to the multidimensional feature of the PES along the bond-dissociation RC, as demonstrated in Figure 11. As discussed previously, the initial femtosecond wave packet prepared on the S_1 surface would involve three vibrational degrees of freedom, namely the CO stretching, the CO out-of-plane wagging, and the ring-puckering modes. The excess energy ($\sim$6 kcal mol^{-1}) originally deposited in these vibrational modes has to be transferred into the initially optical-inactive, asymmetric α-CC bond-stretching mode through IVR. The fundamental vibrational frequency of this asymmetric ring-stretching mode was calculated to be 1152 cm^{-1} (ν_{18}), which is similar to the energy barrier required (700–1300 cm^{-1})[14] to overcome the transition state on the S_1 surface along the α-cleavage RC. This indicates that a single quantum of the ν_{18} vibrational energy is sufficient for the S_1 species to cross the barrier. Therefore, the observed S_1 dynamics should correspond to the time scale of the IVR process, which is on the order of 1–100 ps. The redistribution of the internal energy from the initially activated out-of-plane bending modes into the in-plane ring-opening reaction coordinate defines the time scale for IVR, and the observed ps-scale decay gives the rate of IVR/α-cleavage across the barrier on the S_1 surface.

4.4. Isotope Effect

The observed significant isotope effect for the S_1 lifetime, $\tau([D_4]CB)/\tau([D_0]CB) = 1.4$ and $\tau([D_2]CB)/\tau([D_0]CB) = 1.8$, is consistent with our dynamic picture, that the CO out-of-plane wagging and the ring-puckering motions are involved during IVR prior to dissociation. The even slower S_1 dynamics observed for $[D_2]$CB as compared to others indicate the relevance of the vibrational coupling between the ring-puckering mode and the α-CC bond-dissociation RC. According to the spectroscopic data analyses,[16] a substantial energy barrier (for example, 2150 cm^{-1}) is involved in the motion of the CO out-of-plane inversion while the motion along the ring-puckering coordinate is essentially barrierless. This evidence indicates that the ring-puckering motion in the S_1 state is more important for the observed dynamics than the other motions. According to our frequency calculations (Figure 8B), the normal-coordinate vectors of two relevant modes (a′) involve substantial movements of the hydrogen atoms located in the C_2 and C_4, as well as the C_3, positions. Therefore, the replacement of the hydrogen atoms by deuterium on those positions is expected to retard the S_1 dynamics, as we have observed. The observed isotope effect further highlights the significance of the ring-puckering motion for the S_1 dynamics of cyclobutanone along the α-cleavage reaction pathway.

5. Conclusion

Based on our experimental and theoretical findings, a dynamic model for the observed femto- and picosecond dynamics of cyclobutanone taking place on the S_1 potential energy surface has been deduced and is summarized as follows.

a) Upon excitation by a femtosecond laser pulse at $\lambda_{ex} = 307$ nm, cyclobutanone is promoted to the $S_1(n,\pi^*)$ state. This excitation activates three vibrational modes corresponding to the CO out-of-plane wagging, the ring puckering, and the CO stretching motions.
b) The initial dephasing occurs in less than 50 fs. This result indicates that the fs wave packet initially prepared on the S_1 surface is rapidly propagating out of the Franck–Condon region within a vibrational period. The S_1 equilibrium geometry is highly bent and pyramidal with elongation of the CO bond. Therefore, the driving force for the ultrafast dephasing process is the corresponding CO bond-stretching

and the CO out-of-plane wagging (pyramidalization) motions.

c) The energy barrier of the α-CC bond-dissociation channel on the S_1 surface is as low as ~ 2 kcal mol^{-1}. Therefore, the excess energy (~ 6 kcal mol^{-1}) is sufficient to break the α-CC bond after IVR from the originally active vibrational modes into the relevant α-CC stretching mode, which gives rise to an efficient nonradiative predissociation channel.

d) The observed 5 ps for the overall S_1 dynamics of CB is consistent with our IVR picture (Figure 11), and, strikingly, the ps time scale responsible for its S_1 lifetime is shorter by three orders of magnitude than the lifetime observed for other aliphatic ketones at the same or even much higher excitation energies.[1, 14] Such an anomalous dynamic behavior is due to the extremely low energy barrier of CB along the S_1 α-CC bond-breaking (ring-opening) RC.

e) The observed prominent isotope effect for both [D_2]- and [D_4]CB indicates that the active vibrational modes, in particular the ring-puckering motion, play a key role for the observed S_1 dynamics.

f) Following the α-bond-breaking reaction path through the energy barrier on the S_1 surface down to the S_0 surface via the S_0/S_1 CI, the structural changes at each stationary point along the pathway are substantial. In particular, the CCO bending angle changes considerably: 133° at the S_1 Franck–Condon region to 122° at the S_1 minimum, increasing to 136° at the S_1 transition state, and becoming 173° when reaching the S_0/S_1 CI region. The relevant vibrational motions, which involve the drastic change of the CCO bending angle, must play a role for the dynamics of the entire carbonyl family in the Norrish type-I reactions.[1]

g) Our theoretical calculations indicate the ground-state reaction paths to be followed after funneling through the S_0/S_1 CI: The nonadiabatic coupling vector $\boldsymbol{x}_2$ corresponds to a motion leading to either a hot S_0 species or a diradical intermediate (giving C_2 products), whereas the gradient difference vector $\boldsymbol{x}_1$ corresponds to the formation of trimethylene and CO or hot cyclopropane and CO (C_3 products). The proposed dynamic picture for the photochemistry of cyclobutanone on the S_1 surface not only can account for the abnormally sharp decrease in Φ_F and τ_F but also for the dramatic change in the C_3:C_2 product ratio as a function of increasing excitation energy, as reported by Lee and co-workers.[14]

This work was supported by the Office of Naval Research and the US Air Force Office of Scientific Research. C.K., a Feodor Lynen Fellow from the Alexander von Humboldt Foundation, acknowledges the Foundation and Caltech for support. We thank Prof. John E. Baldwin for many helpful discussions and Dr. Rajesh Shukla and Mr. Dharmesh B. Patel for preparation of the deuterium-labeled cyclobutanones; the relevance of the diradical work will be published separately. We are grateful to Prof. Joseph Casanova and Dr. Theis I. Sølling for helpful discussions. E.W.-G.D. would like to acknowledge Prof. Ching-Han Hu for his many helpful suggestions and discussions.

[1] E. W.-G. Diau, C. Kötting, A. H. Zewail, *Chem. Phys. Chem.* **2001**, *2*, 273–293, the preceding paper in this issue.
[2] W. A. Noyes, Jr. in *Photochemistry and Reaction Kinetics* (Eds.: P. G. Ashmore, F. S. Dainton, T. M. Sugden), Cambridge University Press, Cambridge, **1967**, pp. 1–25.
[3] C. Bohne in *CRC Handbook of Organic Photochemistry and Photobiology* (Eds.: W. M. Horspool, P.-S. Song), CRC, New York, NY, **1995**, pp. 416–429, and references therein.
[4] J. C. Dalton, N. J. Turro, *Ann. Rev. Phys. Chem.* **1970**, *31*, 499–560; also see N. J. Turro, *Modern Molecular Photochemistry*, University Science Books, Sausalito, CA, **1991**.
[5] J. Michl, V. Bonaic-Koutecky, *Electronic Aspects of Organic Photochemistry*, Wiley, New York, NY, **1990**.
[6] M. Reinsch, M. Klessinger, *J. Phys. Org. Chem.* **1990**, *3*, 81–88; also see M. Klessinger, J. Michl, *Excited States and Photochemistry of Organic Molecules*, VCH, New York, NY, **1995**.
[7] E. K. C. Lee, R. S. Lewis, *Adv. Photochem.* **1980**, *12*, 1–95, and references therein.
[8] S. J. Formosinho, L. G. Arnaut, *Adv. Photochem.* **1991**, *16*, 67–117.
[9] N. J. Turro, J. C. Dalton, K. Dawes, G. Farrington, R. Hautala, D. Morton, M. Niemczyk, N. Schore, *Acc. Chem. Res.* **1972**, *5*, 92–101, and references therein for the studies in solutions.
[10] E. K. C. Lee, *Acc. Chem. Res.* **1977**, *10*, 319–326, and references therein for the gas-phase studies.
[11] G. S. Hammond, *J. Am. Chem. Soc.* **1955**, *77*, 334–338.
[12] L. Salem, *J. Am. Chem. Soc.* **1974**, *96*, 3486–3501.
[13] N. J. Turro, W. E. Farenth, A. Devaquet, *J. Am. Chem. Soc.* **1976**, *98*, 7425–7427.
[14] a) H. O. Denschlag, E. K. C. Lee, *J. Am. Chem. Soc.* **1968**, *90*, 3628–3638; b) N. E. Lee, E. K. C. Lee, *J. Chem. Phys.* **1969**, *50*, 2094–2107, and references therein; c) J. C. Hemminger, C. F. Rusbult, E. K. C. Lee, *J. Am. Chem. Soc.* **1971**, *93*, 1867–1871; d) G. M. Breuer, E. K. C. Lee, *J. Phys. Chem.* **1971**, *75*, 989–990; e) J. C. Hemminger, E. K. C. Lee, *J. Chem. Phys.* **1972**, *56*, 5284–5295; f) K. Y. Tang, E. K. C. Lee, *J. Phys. Chem.* **1976**, *80*, 1833–1836.
[15] M. Baba, I. Hanazaki *J. Chem. Phys*. **1984**, *81*, 5426–5433.
[16] a) J. Zhang, W.-Y. Chiang, J. Laane, *J. Chem. Phys.* **1994**, *100*, 3455–3562; b) P. A. Sagear, S. N. Lee, J. Laane, *J. Chem. Phys.* **1997**, *106*, 3876–3883.
[17] K. A. Trentelman, D. B. Moss, S. H. Kable, P. L. Houston, *J. Phys. Chem.* **1990**, *94*, 3031–3039, and references therein.
[18] D. C. Moule, *J. Chem. Phys.* **1976**, *64*, 3161–3168.
[19] J. C. Hemminger, H. A. J. Carless, E. K. C. Lee, *J. Am. Chem. Soc.* **1973**, *95*, 682–685.
[20] D. A. Hansen, E. K. C. Lee, *J. Chem. Phys.* **1975**, *62*, 183–189.
[21] R. J. Campbell, E. W. Schlag, B. W. Ristow, *J. Am. Chem. Soc.* **1967**, *89*, 5098–5102.
[22] J. Zhang, W.-Y. Chiang, J. Laane, *J. Chem. Phys.* **1993**, *98*, 6129–6137.
[23] D. J. Tozer, N. C. Handy, *Phys. Chem. Chem. Phys*. **2000**, *2*, 2117–2121, and references therein.
[24] *Gaussian 98* (*Rev. A.9*), M. J. Frisch, G. W. Trucks, H. B. Schlegel, G. E. Scuseria, M. A. Robb, J. R. Cheeseman, V. G. Zakrzewski, J. A. Montgomery, R. E. Stratmann, J. C. Burant, S. Dapprich, J. M. Millam, A. D. Daniels, K. N. Kudin, M. C. Strain, O. Farkas, J. Tomasi, V. Barone, M. Cossi, R. Cammi, B. Mennucci, C. Pomelli, C. Adamo, S. Clifford, J. Ochterski, G. A. Petersson, P. Y. Ayala, Q. Cui, K. Morokuma, D. K. Malick, A. D. Rabuck, K. Raghavachari, J. B. Foresman, J. Cioslowski, J. V. Ortiz, B. B. Stefanov, G. Liu, A. Liashenko, P. Piskorz, I. Komaromi, R. Gomperts, R. L. Martin, D. J. Fox, T. Keith, M. A. Al-Laham, C. Y. Peng, A. Nanayakkara, C. Gonzalez, M. Challacombe, P. M. W. Gill, B. G. Johnson, W. Chen, M. W. Wong, J. L. Andres, M. Head-Gordon, E. S. Replogle, J. A. Pople, Gaussian, Inc., Pittsburgh, PA, **1998**.
[25] A. D. Becke, *J. Chem. Phys.* **1993**, *98*, 5648–5652.
[26] C. Lee, W. Yang, R. G. Parr, *Phys. Rev. B* **1988**, *37*, 785.
[27] W. Hehre, L. Radom, P. von R. Schleyer, J. A. Pople, *Ab Initio Molecular Orbital Theory*, Wiley, New York, NY, **1986**.
[28] E. W.-G. Diau, J. Casanova, J. D. Roberts, A. H. Zewail, *Proc. Natl. Acad. Sci. USA* **2000**, *97*, 1376–1379.
[29] F. Dubnikova, A. Lifshitz, *J. Phys. Chem. A* **1998**, *102*, 3299–3306.
[30] H. F. Bettinger, J. C. Rienstra-Kiracofe, B. C. Hoffman, H. F. Schaefer III, J. E. Baldwin, P. von R. Schleyer, *Chem. Commun.* **1999**, *16*, 1515–1516.

[31] M. N. Das, F. Kern, T. D. Coyle, W. D. Walters, *J. Am. Chem. Soc.* **1954**, *76*, 6271 – 6274.
[32] R. B. Woodward, R. Hoffmann, *Angew. Chem.* **1969**, *81*, 797 – 869; *Angew. Chem. Int. Ed. Engl.* **1969**, *8*, 781 – 932.
[33] X. Wang, K. N. Houk, *J. Am. Chem. Soc.* **1990**, *112*, 1754 – 1756.
[34] F. Bernardi, A. Bottoni, M. A. Robb, A. Venturini, *J. Am. Chem. Soc.* **1990**, *112*, 2106 – 2114.
[35] P. Yates, R. Loutfy, *Acc. Chem. Res.* **1975**, *8*, 209 – 216.
[36] P. Engel, *Chem. Rev.* **1980**, *80*, 99 – 150.
[37] M. Merchan, B. O. Roos, R. McDiardmid, X. Xing, *J. Chem. Phys.* **1996**, *104*, 1791 – 1804.
[38] D. W. Liao, A. M. Mebel, M. Hayashi, Y. J. Shiu, Y. T. Chen, S. H. Lin, *J. Chem. Phys.* **1999**, *111*, 205 – 215.
[39] J. P. Perdew, *Phys. Rev. B* **1986**, *23*, 8822.
[40] L. O'Toole, P. Brint, C. Kosmidis, G. Boulakis, P. Tsekeris, *J. Chem. Soc. Faraday Trans.* **1991**, *87*, 3343 – 3351.
[41] The equilibrium geometry of the $S_1(C_1)$ species of CB is characterized by two different α-CC bond length (1.523 and 1.569 Å) with both CO out-of-plane wagging and ring-puckering angles similar to those of $S_1(C_s)$. The calculated energies of $S_1(C_1)$ are summarized in Table 2.
[42] K. Frei, H. H. Günthard, *J. Mol. Spectrosc.* **1960**, *5*, 218 – 235.
[43] T. R. Borgers, H. L. Strauss, *J. Chem. Phys.* **1966**, *45*, 947 – 955.
[44] For the $S_0(C_{2v})$ species, the frequencies calculated at the B3LYP/6-31G(d) level are, on average, slightly overestimated by $\sim$2% and those computed at the CASSCF(10,8)/6-31G(d) level overestimated by $\sim$8% in comparison with the experimental values (Table 3). Note that both ν_{13} and ν_{27} modes are excluded from the comparison because the former is uncertain in the spectroscopy assignments and the latter involves large uncertainties from calculations. In fact, the scaling factors of vibrational frequency used for predicting the vibronic spectra of acetone are 0.9614 and 0.93 for the B3LYP and CASSCF methods, respectively.[38]
[45] To demonstrate the effect of ring strain with respect to the α-cleavage ring-opening process for a cyclic ketone, we have also carried out the same quantum chemical calculations for a five-membered ring ketone, cyclopentanone (CP). The S_1 ring-opening barrier height of CP was calculated to be 10.9 kcal mol^{-1} at the TD-B3P86/6-311++G(d,p)//CAS(10,8)/6-31G(d) level of theory, where the value is substantially higher than that of CB as discussed in the text. Furthermore, at the saddle point (S_1-TS) the stretched α-CC bond length of CP was determined to be 1.996 Å, which is also considerably longer than that of CB (1.862 Å). The calculated energies for CP at the $S_0(C_2)$, $S_1(C_1)$, and S_1-TS equilibrium structures have been reported elsewhere.[1]
[46] I. N. Ragazos, M. A. Robb, F. Bernardi, M. Olivucci, *Chem. Phys. Lett.* **1992**, *197*, 217 – 223.
[47] W. Domcke, G. Stock, *Adv. Chem. Phys.* **1997**, *100*, 1.
[48] D. R. Yarkony, *Acc. Chem. Res.* **1998**, *31*, 511 – 518.
[49] M. Klessinger, *Angew. Chem.* **1995**, *107*, 597 – 599; *Angew. Chem. Int. Ed. Engl.* **1995**, *34*, 549 – 551.
[50] F. Bernardi, M. Olivucci, M. A. Robb, *Chem. Soc. Rev.* **1996**, *25*, 321 – 328, and references therein.
[51] S. Wilsey, K. N. Houk, A. H. Zewail, *J. Am. Chem. Soc.* **1999**, *121*, 5772 – 5786, and references therein.
[52] a) E. W.-G. Diau, O. K. Abou-Zied, A. A. Scala, A. H. Zewail, *J. Am. Chem. Soc.* **1998**, *120*, 3245 – 3246; b) E. W.-G. Diau, S. De Feyter, A. H. Zewail, *Chem. Phys. Lett.* **1999**, *304*, 134 – 144; c) S. De Feyter, E. W.-G. Diau, A. H. Zewail, *Phys. Chem. Chem. Phys.* **2000**, *2*, 877 – 883.
[53] A signal is saturated by the I_{pump} if the pump-laser power dependence of the signal differs from that at very low I_{pump}. Under the saturated conditions, however, the slightly distorted shape of a transient does not lead to additional features, such as changing the underlying nature of the transient. For more detailed discussion regarding the effect of pump (or probe) saturation, see S. Pedersen, A. H. Zewail, *Mol. Phys.* **1996**, *89*, 1455 – 1502.
[54] A. H. Zewail, *Femtochemistry: Ultrafast Dynamics of the Chemical Bond*, *Vol. I and II*, World Scientific, Singapore, **1994**, and references therein.
[55] E. W.-G. Diau, S. De Feyter, A. H. Zewail, *J. Chem. Phys.* **1999**, *110*, 9785 – 9788.
[56] D. Zhong, E. W.-G. Diau, T. M. Bernhardt, S. De Feyter, J. D. Roberts, A. H. Zewail, *Chem. Phys. Lett.* **1998**, *298*, 129 – 140.
[57] J. E. Baldwin, D. B. Patel, *J. Labelled Compd. Radiopharm.* **1999**, *42*, 55 – 61.
[58] W. J. Leigh, J. A. Postigo, *Can. J. Chem.* **1995**, *73*, 191 – 203.

Received: December 29, 2000 [F172]